Journal of Sound and Vibration (2001) **239**(4), 607–637
doi:10.1006/jsvi.2000.3227, available online at http://www.idealibrary.com on IDEAL®

SPHERICAL HARMONICS, SINGULAR-VALUE DECOMPOSITION AND THE HEAD-RELATED TRANSFER FUNCTION

P. A. Nelson and Y. Kahana

Institute of Sound and Vibration Research, University of Southampton, Southampton SO17 1BJ, England. E-mail: pan@isvr.soton.ac.uk

(*Accepted* 29 *August* 2000)

The singular-value decomposition (SVD) can be used to analyze the matrix of Green functions relating the acoustic pressure at a number of field points to the strengths of a number of point sources on the surface of a body which radiates or scatters sound. The left and right singular vectors of the resulting decomposition yield, at a given frequency, two sets of orthogonal basis functions describing "field mode shapes" and "source mode shapes" respectively. This paper attempts to make the connection between this decomposition and the basis functions of classical acoustics. In particular, it is found that for a spherical co-ordinate system, when the source points and field points are chosen in order to sample the source and field appropriately, then the matrices of left and right singular vectors are related to the sampled spherical harmonics by a unitary transformation. Preliminary investigations are presented of the sensitivity of this relationship to the manner in which the source and field are sampled. In addition, the great utility of the method is illustrated with some new results of numerical analysis of the scattering of sound by the outer ear. "Pinna resonances" and their associated "mode shapes" are identified at certain frequencies where high values of the dominant singular values indicate a strong coupling between source and field.

1. INTRODUCTION

The singular-value decomposition (SVD) has for some years been recognized as a useful mathematical tool for analyzing problems in sound radiation and scattering. With regard to sound radiation problems, Borgiotti showed [1] in a very general way that, at a given frequency, the "radiation operator" relating the velocity on the surface of a vibrating body to the sound pressure produced over a surface in the radiated field could be advantageously decomposed by using a singular function representation. Photiadis [2] also pointed out the utility of the SVD when the radiation operator involved is a matrix of Green functions relating a number of points on the surface of the body to a number of points in the sound field. The left and right singular vectors of the SVD of the Green function matrix yield two sets of basis functions which, respectively, represent a series of mutually orthogonal complex "field mode shapes" and mutually orthogonal complex "source mode shapes". Each of the field mode shapes is related to only one of the source mode shapes by a single real number corresponding to the relevant singular value in the SVD. These ideas were further exploited by Currey and Cunefare [3] and Elliott and Johnson [4], the latter computing the "radiation modes" of a simply supported baffled plate. All of these authors emphasized the fact that the "source mode shapes" contribute orthogonally to the total

0022-460X/01/040607 + 31 $35.00/0

radiated sound power over the surface considered. The SVD has also been used extensively in the study of inverse acoustic radiation and scattering problems. For example, Veronesi and Maynard [5] formulated the source strength reconstruction problem in this way and the technique has been used in this context by a number of authors (see, for example, Filippi *et al.* [6], Kim and Lee [7], Grace *et al.* [8, 9], Nelson and Yoon [10, 11] and Nelson [12]). The SVD is of course central to the solution of inverse scattering problems not only in acoustics, but also, for example, in electromagnetic theory and the reader is referred to the excellent text by Colton and Kress [13] for an in-depth treatment of these problems.

Of course, the use of a set of orthogonal basis functions for describing acoustic fields is in itself a truly classical notion [14–16] and the principal objective of this paper is to explore further the relationship between the results of the application of the SVD and the long-established basis functions of classical acoustics. The paper therefore begins by attempting to further understand the connection between the "mode shapes" yielded by the SVD and the series of spherical harmonics used to describe sound radiation from a vibrating spherical surface. The study proceeds by re-deriving the Green function for this problem in terms of the complex spherical harmonics and then using this solution to compute the Green function matrix relating a number of points on the surface to a number of points in the far field. The results of the SVD of this matrix are then found to be related to the spherical harmonic basis functions by a unitary transformation and thus the "mode shape" yielded by the SVD for this problem are shown to be linear combinations of spherical harmonics of a given order.

The paper goes on to explore the effect of changing the shape of the radiating body from a sphere to an ellipsoid. In this case, a boundary element code is used to generate the relevant Green function matrix and the results illustrate the departure of the "source mode shapes" from the classical spherical harmonics, whilst the singular values are no longer grouped in spherical harmonic order as is the case for the sphere. Finally, as an illustration of the great utility of the SVD in analyzing scattering problems, some results are presented of the numerical simulation of the Green function matrix relating points on the surfaces of a model of the human pinna mounted on a rigid baffle and points on a hemisphere in the far field. The resulting SVD yields dominant singular values at certain frequencies and the associated "mode shapes" are found to clearly illustrate the spatial functions identified from previous experimental studies as those associated with "pinna resonance" [17–19].

2. THEORY

2.1. SOLUTIONS OF THE WAVE EQUATION IN SPHERICAL CO-ORDINATES

The scalar Helmholtz equation governing the behaviour of the complex acoustic pressure $p(\mathbf{r})$ is given by

$$(\nabla^2 + k^2)p(\mathbf{r}) = 0 \tag{1}$$

and when written in spherical co-ordinates (r, θ, ϕ) becomes

$$\frac{1}{r^2}\frac{\partial}{\partial r}\left(r^2\frac{\partial p}{\partial r}\right) + \frac{1}{r^2\sin\theta}\frac{\partial}{\partial\theta}\left(\sin\theta\frac{\partial p}{\partial\theta}\right) + \frac{1}{r^2\sin^2\theta}\frac{\partial^2 p}{\partial\phi^2} + k^2 p = 0. \tag{2}$$

Since this equation is separable, then assuming a solution of the form $p(\mathbf{r}) = F(r)G(\theta)H(\phi)$ yields three ordinary differential equations, respectively, governing the radial, polar and

azimuthal dependence of the acoustic pressure. These are given by [15, 20]

$$r^2 \frac{d^2F}{dr^2} + 2r \frac{dF}{dr} + (k^2r^2 - C^2)F = 0, \qquad \frac{1}{\sin\theta} \frac{d}{d\theta}\left(\sin\theta \frac{dG}{d\theta}\right) + \left(C^2 - \frac{m^2}{\sin^2\theta}\right) G = 0, \quad (3, 4)$$

$$d^2H/d\phi^2 + m^2H = 0, \quad (5)$$

where C^2 and m^2 are the separation constants. First note that the solutions of equation (5) are given by $e^{\pm jm\phi}$ where $j = \sqrt{-1}$, but that m must be a positive or negative integer ($m = 0, \pm 1, \pm 2 \ldots$) if the pressure is to be a single-valued function of ϕ (i.e., to ensure that $p(r, \theta, \phi + 2\pi) = p(r, \theta, \phi)$). It can also be argued [20] that for equation (4) to have solutions that are finite at $\theta = 0$ and π then $C = n(n+1)$ where n must be a positive integer ($n = 0, 1, 2, \ldots$). The solutions of equation (4) when $m = 0$ are given by the Legendre polynomials $P_n(\cos\theta)$. For non-zero m, the solution is given by the associated Legendre polynomials $P_n^m(\cos\theta)$ defined by

$$P_n^m(x) = \frac{1}{2^n n!}(1 - x^2)^{m/2} \frac{d^{m+n}}{dx^{m+n}}(x^2 - 1)^n, \quad -n \leqslant m \leqslant n. \quad (6)$$

Note that this definition (used by Arfken [16]) enables the inclusion of both positive and negative values of m. Also note that it can be shown that [16]

$$P_n^{-m}(x) = (-1)^m ((n-m)!/(n+m)!)\, P_n^m(x). \quad (7)$$

The polar and azimuthal dependences of the pressure are combined in the definition of the spherical harmonics given by [16]

$$Y_n^m(\theta, \phi) = (-1)^m \sqrt{(2n+1)(n-m)!/4\pi(n+m)!}\, P_n^m(\cos\theta) e^{jm\phi}. \quad (8)$$

These spherical harmonics satisfy the orthogonality condition

$$\int_0^{2\pi} \int_0^{\pi} Y_n^{m*}(\theta, \phi)\, Y_k^l(\theta, \phi) \sin\theta \, d\theta \, d\phi = \delta_{nk}\delta_{ml}, \quad (9)$$

where $\delta_{nk} = 1$ for $n = k$ and $\delta_{nk} = 0$ for $n \neq k$ and δ_{ml} is analogously defined. It should also be noted that following Arfken the factor $(-1)^m$ has been included and constitutes a phase term (the "Condon–Shortley phase") which has the effect of introducing an alternation of sign among the spherical harmonics corresponding to positive m. Finally, the functions describing the radial dependence of the acoustic pressure that satisfy equation (3) are given by the spherical Hankel functions of order n defined by

$$h_n^{(1)}(kr) = j_n(kr) + jn_n(kr), \qquad h_n^{(2)}(kr) = j_n(kr) - jn_n(kr), \quad (10, 11)$$

where $j_n(kr)$ and $n_n(kr)$ are, respectively, the spherical Bessel and Neumann functions of order n. These are in turn related to the Bessel function of order $(n + 1/2)$ and Neumann function of order $(n + 1/2)$ by

$$j_n(kr) = \sqrt{\pi/2kr}\, J_{n+1/2}(kr), \qquad n_n(kr) = \sqrt{\pi/2kr}\, N_{n+1/2}(kr). \quad (12, 13)$$

The spherical Hankel functions can also be deduced from [16]

$$h_n^{(1)}(x) = -j(-1)^n x^n \left(\frac{d}{x\,dx}\right)^n \left(\frac{e^{jx}}{x}\right), \qquad h_n^{(2)}(x) = j(-1)^n x^n \left(\frac{d}{x\,dx}\right)^n \left(\frac{e^{-jx}}{x}\right). \quad (14, 15)$$

It therefore follows that for $n = 0$, for example,

$$h_0^{(1)}(kr) = -je^{jkr}/kr, \qquad h_0^{(2)}(kr) = je^{-jkr}/kr \quad (16a, b)$$

which define either incoming or outgoing waves depending upon the choice of time convention.

2.2. RADIATION FROM A POINT SOURCE ON A RIGID SPHERE

The sound field produced by a point source situated at a vector position $\mathbf{r}_0$ in an otherwise unbounded medium is described by the free-space Green function $g(\mathbf{r}|\mathbf{r}_0)$ which is a solution of

$$(\nabla^2 + k^2)g(\mathbf{r}|\mathbf{r}_0) = -\delta(\mathbf{r} - \mathbf{r}_0). \quad (17)$$

When a harmonic time dependence of $e^{j\omega t}$ is assumed, the free-space Green function describing waves propagating outwards from $\mathbf{r}_0$ is given by

$$g(\mathbf{r}|\mathbf{r}_0) = e^{-jk|\mathbf{r}-\mathbf{r}_0|}/4\pi|\mathbf{r} - \mathbf{r}_0|\,. \quad (18)$$

This function can be expressed in terms of a series expansion of the spherical harmonics described above (see, for example, references [16, Chapter 16, p. 768, 14, Chapter 11, p. 1466], or [15, Chapter 7, p. 352]). This series expansion can be written as

$$g(\mathbf{r}|\mathbf{r}_0) = -jk \sum_{n=0}^{\infty} j_n(kr_0)h_n^{(2)}(kr) \sum_{m=-n}^{n} Y_n^m(\theta, \phi)Y_n^{m*}(\theta_0, \phi_0) \quad (r > r_0), \quad (19)$$

where $r = |\mathbf{r}|$ and $r_0 = |\mathbf{r}_0|$ and * denotes the complex conjugate. This series expansion differs slightly from that given in reference [15] since an $e^{j\omega t}$ time dependence has been assumed and thus $h_n^{(2)}(kr)$ has been used in place of $h_n^{(1)}(kr)$. See also reference [13, Chapter 2, p. 30] for a rigorous proof of this relationship. As shown by Morse and Ingard [15, Chapter 7, p. 355] this series expansion can be used to construct the Green function $G(\mathbf{r}|\mathbf{r}_0)$ describing radiation from a point source on the surface of an otherwise rigid sphere. Formally speaking, this is accomplished by adding to $g(\mathbf{r}|\mathbf{r}_0)$ a further function $\chi(\mathbf{r})$ which satisfies the homogeneous Helmholtz equation $(\nabla^2 + k^2)\chi(\mathbf{r}) = 0$ and which ensures that the radial gradient of the sum of $g(\mathbf{r}|\mathbf{r}_0)$ and $\chi(\mathbf{r})$ is zero at the surface of the sphere. Following Morse and Ingard [15], the Green function satisfying these conditions can be written as

$$G(\mathbf{r}|\mathbf{r}_0) = -jk \sum_{n=0}^{\infty} \left[\frac{j_n(kr_0)h_n^{(2)'}(ka) - j_n'(ka)h_n^{(2)}(kr_0)}{h_n^{(2)'}(ka)}\right] h_n^{(2)}(kr)$$

$$\times \sum_{m=-n}^{n} Y_n^m(\theta, \phi)Y_n^{m*}(\theta_0, \phi_0), \quad (20)$$

where a is the radius of the sphere and the prime denotes differentiation with respect to the argument.

The inhomogeneous Helmholtz equation given by

$$(\nabla^2 + k^2)p(\mathbf{r}) = -Q_{vol}(\mathbf{r}_0), \tag{21}$$

where $Q_{vol}(\mathbf{r}_0)$ represents some volume source distribution, has the general solution

$$p(\mathbf{r}) = \int_V Q_{vol} G(\mathbf{r}|\mathbf{r}_0)\,\mathrm{d}V + \int_S [G(\mathbf{r}|\mathbf{r}_0)\nabla_0 p(\mathbf{r}_0) - p(\mathbf{r}_0)\nabla_0 G(\mathbf{r}|\mathbf{r}_0)]\,.\,\mathbf{n}\,\mathrm{d}S, \tag{22}$$

where S is the surface with unit outward normal vector $\mathbf{n}$ that bounds the volume V containing the field point $\mathbf{r}$, and ∇_0 is the gradient operator with respect to the co-ordinates defined by $\mathbf{r}_0$. Since $G(\mathbf{r}|\mathbf{r}_0)$ given by equation (20) has been chosen to satisfy $\nabla_0 G(\mathbf{r}|\mathbf{r}_0)\mathbf{n} = 0$ on the surface of the sphere, and if there are no other sources within V, then

$$p(\mathbf{r}) = \int_S G(\mathbf{r}|\mathbf{r}_0)\nabla_0 p(\mathbf{r}_0)\,.\,\mathbf{n}\,\mathrm{d}S, \tag{23}$$

where the integration is carried out only over the surface of the sphere. (The other part of S is that part of the surface bounding the volume V outside the sphere and thus lies at infinity; the contribution to the surface integral from this part of S can be shown to zero by virtue of the Sommerfeld radiation condition [15]). If the sphere is now assumed to have an arbitrary radial velocity distribution $\nabla_0 p(\mathbf{r}_0).\mathbf{n} = \mathrm{j}\omega\rho_0 u_n(\theta_0, \phi_0)$ then it follows that

$$p(\mathbf{r}) = \mathrm{j}\omega\rho_0 a^2 \int_0^{2\pi}\int_0^{\pi} G(\mathbf{r}|\mathbf{r}_0)u_n(\theta_0, \phi_0)\sin\theta_0\,\mathrm{d}\theta_0\,\mathrm{d}\phi_0. \tag{24}$$

It therefore follows that the expression for the pressure field generated by an arbitrary surface velocity distribution can be written as

$$p(\mathbf{r}) = \rho_0 c_0 k^2 a^2 \sum_{n=0}^{\infty} \frac{[\mathrm{j}_n(ka)\mathrm{h}_n^{(2)'}(ka) - \mathrm{j}_n'(ka)\mathrm{h}_n^{(2)}(ka)]}{\mathrm{h}_n^{(2)'}(ka)}\,\mathrm{h}_n^{(2)}(kr) \sum_{m=-n}^{n} U_n^m \mathrm{Y}_n^m(\theta, \phi), \tag{25}$$

where the factor U_n^m accounts for the degree to which a given spherical harmonic is driven by a given velocity distribution and is defined by

$$U_n^m = \int_0^{2\pi}\int_0^{\pi} u_n(\theta_0, \phi_0)\mathrm{Y}_n^{m*}(\theta_0, \phi_0)\sin\theta_0\,\mathrm{d}\theta_0\,\mathrm{d}\phi_0. \tag{26}$$

If the velocity distribution is now assumed to be that associated with a point source of strength $q(\hat{\mathbf{r}})$ at $(\hat{\theta}, \hat{\phi})$ where

$$u_n(\theta_0, \phi_0) = -q\,\delta(\theta_0 - \hat{\theta})\delta(\phi_0 - \hat{\phi})/\sin\theta_0\,, \tag{27}$$

then U_n^m is simply given by $-q\mathrm{Y}_n^{m*}(\hat{\theta}, \hat{\phi})$. Furthermore, since [16, see p. 529]

$$\mathrm{j}_n(x)n_n'(x) - \mathrm{j}_n'(x)n_n(x) = (1/x^2) \tag{28}$$

then it can be shown that the term in the square brackets in equation (25) reduces to $-\mathrm{j}/k^2a^2$ and one simply has

$$p(r) = \mathrm{j}\rho_0 c_0 q(\hat{\mathbf{r}}) \sum_{n=0}^{\infty} \frac{\mathrm{h}_n^{(2)}(kr)}{\mathrm{h}_n^{(2)'}(ka)} \sum_{m=-n}^{n} \mathrm{Y}_n^m(\theta, \phi)\mathrm{Y}_n^{m*}(\hat{\theta}, \hat{\phi}). \tag{29}$$

Note that in evaluating the derivative $h_n^{(2)'}(ka)$ one may make use of the result [16]

$$j_n'(x) = (1/(2n+1))\,[nj_{n-1}(x) - (n+1)j_{n+1}(x)]$$

and an exactly analogous expression for $n_n'(x)$.

2.3. THE SINGULAR-VALUE DECOMPOSITION

Now assume that for a given linear acoustic problem it is possible to specify a matrix $\mathbf{G}(\mathbf{r}|\hat{\mathbf{r}})$ of Green functions† relating the pressures produced at a number of field points specified by the position vector $\mathbf{r}$ to the strengths of a number of point sources at positions specified by the position vector $\hat{\mathbf{r}}$. That is to say,

$$\mathbf{p}(\mathbf{r}) = \mathbf{G}(\mathbf{r}|\hat{\mathbf{r}})\mathbf{q}(\hat{\mathbf{r}}), \tag{30}$$

where $\mathbf{p}(\mathbf{r})$ is the vector whose elements define the respective field pressures and $\mathbf{q}(\hat{\mathbf{r}})$ is the vector whose elements define the source strengths. It will now be demonstrated that the singular-value decomposition (SVD) of the matrix $\mathbf{G}(\mathbf{r}|\hat{\mathbf{r}})$ provides an extremely useful basis for understanding acoustic radiation and scattering problems, especially those associated with "complicated" (non-separable) geometries.

The SVD enables any arbitrary complex matrix $\mathbf{G}(\mathbf{r}|\hat{\mathbf{r}})$ of order $(K \times L)$ to be expressed as

$$\mathbf{G}(\mathbf{r}|\hat{\mathbf{r}}) = \mathbf{U}\boldsymbol{\Sigma}\mathbf{V}^{\mathrm{H}}, \tag{31}$$

where $\boldsymbol{\Sigma}$ is the $(K \times L)$ matrix whose entries are zero apart from the diagonal elements σ_i which comprise the singular values of $\mathbf{G}(\mathbf{r}|\hat{\mathbf{r}})$. The superscript H denotes conjugate transpose. If R is the rank of $\mathbf{G}(\mathbf{r}|\hat{\mathbf{r}})$ then the singular values satisfy

$$\sigma_1 \geqslant \sigma_2 \geqslant \cdots \geqslant \sigma_R > 0, \qquad \sigma_{R+1} = \cdots = \sigma_p = 0, \qquad p = \min(K, L). \tag{32}$$

The matrices $\mathbf{U}$ and $\mathbf{V}$ are, respectively, of dimension $(K \times K)$ and $(L \times L)$ and are unitary matrices having the orthogonality properties

$$\mathbf{U}^{\mathrm{H}}\mathbf{U} = \mathbf{U}\mathbf{U}^{\mathrm{H}} = \mathbf{I}, \qquad \mathbf{V}^{\mathrm{H}}\mathbf{V} = \mathbf{V}\mathbf{V}^{\mathrm{H}} = \mathbf{I}. \tag{33a, b}$$

The columns $\mathbf{u}_i$ of the matrix $\mathbf{U}$ and the columns $\mathbf{v}_i$ of the matrix $\mathbf{V}$, respectively, define the left and right singular vectors of $\mathbf{G}(\mathbf{r}|\hat{\mathbf{r}})$. The significance of the singular vectors is that they provide sets of orthogonal basis functions for describing the spatial variation in radiated pressure and their relationship to spatial variations in source strength. Specifically, it follows from equations (30) and (31) that

$$\mathbf{p}(\mathbf{r}) = \mathbf{U}\boldsymbol{\Sigma}\mathbf{V}^{\mathrm{H}}\mathbf{q}(\hat{\mathbf{r}}) \tag{34}$$

and since by virtue of equation (33a), $\mathbf{U}^{-1} = \mathbf{U}^{\mathrm{H}}$, then this expression may be written as

$$\mathbf{U}^{\mathrm{H}}\mathbf{p}(\mathbf{r}) = \boldsymbol{\Sigma}\mathbf{V}^{\mathrm{H}}\mathbf{q}(\hat{\mathbf{r}}). \tag{35}$$

It thus follows that one may write for all $i \leqslant P$ $(P = \min(K, L))$,

$$\mathbf{u}_i^{\mathrm{H}}\mathbf{p}(\mathbf{r}) = \sigma_i \mathbf{v}_i^{\mathrm{H}}\mathbf{q}(\hat{\mathbf{r}}). \tag{36}$$

†Strictly speaking the matrix $\mathbf{G}(\mathbf{r}|\hat{\mathbf{r}})$ is a matrix of transfer impedance relating pressure to volume velocity.

This demonstrates that a specific spatial pattern in the radiated field defined by $\mathbf{u}_i^{\mathrm{H}}\mathbf{p}(\mathbf{r})$ is linearly related to a specific spatial pattern of source strength distribution defined by $\mathbf{v}_i^{\mathrm{H}}\mathbf{q}(\hat{\mathbf{r}})$. These two patterns are related by the singular value σ_i.

2.4. ALTERNATIVE FORMS OF THE GREEN FUNCTION MATRIX

There is also a close relationship between the singular-value decomposition and the series expansions used in the analyses of acoustical problems in separable co-ordinate systems. In particular, this close relationship can be demonstrated for the case of spherical radiation expressed in terms of a series of spherical harmonics. First note that the SVD of the Green function matrix can be expressed in terms of the left and right singular vectors such that

$$\mathbf{G}(\mathbf{r}\,|\,\hat{\mathbf{r}}) = \sum_{i=1}^{P} \sigma_i \mathbf{u}_i \mathbf{v}_i^{\mathrm{H}} \quad (P = \min(K, L)), \tag{37}$$

where the matrix is shown to consist of a linear superposition of P component matrices each defined by the outer product $\mathbf{u}_i\mathbf{v}_i^{\mathrm{H}}$ and weighted in the summation by the singular value σ_i. Now note that one may use equation (29) to define the elements of the Green function matrix $\mathbf{G}(\mathbf{r}\,|\,\hat{\mathbf{r}})$ relating the acoustic pressure at K points in the sound field to the source strength at L points on the surface of a sphere. This matrix can be written in the form

$$\mathbf{G}(\mathbf{r}\,|\,\hat{\mathbf{r}}) = \begin{bmatrix} \sum_{n=0}^{\infty} f_n \sum_{m=-n}^{n} \mathrm{Y}_n^m(\theta_1, \phi_1)\mathrm{Y}_n^{m*}(\hat{\theta}_1, \hat{\phi}_1) & \cdots & \sum_{n=0}^{\infty} f_n \sum_{m=-n}^{n} \mathrm{Y}_n^m(\theta_1, \phi_1)\mathrm{Y}_n^{m*}(\hat{\theta}_L, \hat{\phi}_L) \\ \sum_{n=0}^{\infty} f_n \sum_{m=-n}^{n} \mathrm{Y}_n^m(\theta_2, \phi_2)\mathrm{Y}_n^{m*}(\hat{\theta}_1, \hat{\phi}_1) & \cdots & \sum_{n=0}^{\infty} f_n \sum_{m=-n}^{n} \mathrm{Y}_n^m(\theta_2, \phi_2)\mathrm{Y}_n^{m*}(\hat{\theta}_L, \hat{\phi}_L) \\ \vdots & & \vdots \\ \sum_{n=0}^{\infty} f_n \sum_{m=-n}^{n} \mathrm{Y}_n^m(\theta_K, \phi_K)\mathrm{Y}_n^{m*}(\hat{\theta}_1, \hat{\phi}_1) & \cdots & \sum_{n=0}^{\infty} f_n \sum_{m=-n}^{n} \mathrm{Y}_n^m(\theta_K, \phi_K)\mathrm{Y}_n^{m*}(\hat{\theta}_L, \hat{\phi}_L) \end{bmatrix}, \tag{38}$$

where it follows from equation (29) that

$$f_n = \mathrm{j}\rho_0 c_0 \mathrm{h}_n^{(2)}(kr)/\mathrm{h}_n^{(2)'}(ka). \tag{39}$$

Since each term in the series comprising each element of the matrix is weighted by the same factor f_n, it is possible to write the matrix as a linear superposition of matrices having the form

$$\mathbf{G}(\mathbf{r}\,|\,\hat{\mathbf{r}}) = \sum_{n=0}^{\infty} f_n \sum_{m=-n}^{m} \mathbf{y}_n^m(\mathbf{r}_k)\mathbf{y}_n^{m\mathrm{H}}(\hat{\mathbf{r}}_l), \tag{40}$$

where the vectors are defined as

$$\mathbf{y}_n^{m\mathrm{T}}(\mathbf{r}_k) = [\mathrm{Y}_n^m(\theta_1, \phi_1)\mathrm{Y}_n^m(\theta_2, \phi_2) \cdots \mathrm{Y}_n^m(\theta_K, \phi_K)], \tag{41}$$

$$\mathbf{y}_n^{m\mathrm{T}}(\mathbf{r}_l) = [\mathrm{Y}_n^m(\hat{\theta}_1, \hat{\phi}_1)\mathrm{Y}_n^m(\hat{\theta}_2, \hat{\phi}_2) \cdots \mathrm{Y}_n^m(\hat{\theta}_K, \hat{\phi}_K)]. \tag{42}$$

There are some obvious similarities between the singular-value decomposition expressed in the form of equation (37) and the matrix series given by equation (40). The vector $\mathbf{y}_n^m(\mathbf{r}_k)$

has elements which correspond to the values of the (n, m)th spherical harmonic at each of the points in the radiated field at which the pressure is evaluated. The vector $\mathbf{y}_n^m(\hat{\mathbf{r}}_l)$ has corresponding elements at each of the points on the surface of the sphere at which the source strength is evaluated. The vectors $\mathbf{y}_n^m(\mathbf{r}_k)$ thus define the basis functions for the pressure field in much the same way as the vectors $\mathbf{u}_i$. Similarly, the vectors $\mathbf{y}_n^m(\mathbf{r}_k)$ define the basis functions for the source strength distribution in an analogous manner to the vectors $\mathbf{v}_i$. One should note, however, that one would not necessarily expect an exact correspondence between the matrix series given by equation (40) and the SVD in equation (37). Most obviously, the weighting factors differ in that the singular values σ_i are purely real whilst the coefficients f_n are in general complex. Furthermore, the matrix series in equation (40) is infinite, whilst the matrix series representation of the SVD is finite and consists of $P = \min(K, L)$ terms.

However, there is a connection between the two descriptions of the Green function matrix. Note that if one chooses to represent the Green functions in equation (38) as a sum up to a maximum number of $n = N$ spherical harmonics, then the truncated Green function matrix $\mathbf{G}_N(\mathbf{r}|\hat{\mathbf{r}})$ can be expressed as the matrix product

$$\mathbf{G}_N(\mathbf{r}|\hat{\mathbf{r}}) = \mathbf{Y}(\mathbf{r}_k)\mathbf{F}\mathbf{Y}^{\mathrm{H}}(\hat{\mathbf{r}}_l), \tag{43}$$

where the columns of $\mathbf{Y}(\mathbf{r}_k)$ are given by the vectors $\mathbf{y}_n^m(\mathbf{r}_k)$ and the columns of $\mathbf{Y}(\hat{\mathbf{r}}_l)$ are given by the vectors $\mathbf{y}_n^m(\hat{\mathbf{r}}_l)$. The matrix $\mathbf{F}$ is a diagonal matrix consisting of the coefficients f_n. To make clear the structure of these matrices, in the case $N = 1$, $K = 5$ and $L = 3$, the Green function matrix can be expanded as

$$\mathbf{G}_N(\mathbf{r}|\hat{\mathbf{r}}) = \begin{bmatrix} \mathrm{Y}_0^0(\theta_1, \phi_1) & \mathrm{Y}_1^{-1}(\theta_1, \phi_1) & \mathrm{Y}_1^0(\theta_1, \phi_1) & \mathrm{Y}_1^1(\theta_1, \phi_1) \\ \mathrm{Y}_0^0(\theta_2, \phi_2) & \mathrm{Y}_1^{-1}(\theta_2, \phi_2) & \mathrm{Y}_1^0(\theta_2, \phi_2) & \mathrm{Y}_1^1(\theta_2, \phi_2) \\ \mathrm{Y}_0^0(\theta_3, \phi_3) & \mathrm{Y}_1^{-1}(\theta_3, \phi_3) & \mathrm{Y}_1^0(\theta_3, \phi_3) & \mathrm{Y}_1^1(\theta_3, \phi_3) \\ \mathrm{Y}_0^0(\theta_4, \phi_4) & \mathrm{Y}_1^{-1}(\theta_4, \phi_4) & \mathrm{Y}_1^0(\theta_4, \phi_4) & \mathrm{Y}_1^1(\theta_4, \phi_4) \\ \mathrm{Y}_0^0(\theta_5, \phi_5) & \mathrm{Y}_1^{-1}(\theta_5, \phi_5) & \mathrm{Y}_1^0(\theta_5, \phi_5) & \mathrm{Y}_1^1(\theta_5, \phi_5) \end{bmatrix} \begin{bmatrix} f_0 & 0 & 0 & 0 \\ 0 & f_1 & 0 & 0 \\ 0 & 0 & f_1 & 0 \\ 0 & 0 & 0 & f_1 \end{bmatrix}$$

$$\times \begin{bmatrix} \mathrm{Y}_0^{0*}(\hat{\theta}_1, \hat{\phi}_1) & \mathrm{Y}_0^{0*}(\hat{\theta}_2, \hat{\phi}_2) & \mathrm{Y}_0^{0*}(\hat{\theta}_3, \hat{\phi}_3) \\ \mathrm{Y}_1^{-1*}(\hat{\theta}_1, \hat{\phi}_1) & \mathrm{Y}_1^{-1*}(\hat{\theta}_2, \hat{\phi}_2) & \mathrm{Y}_1^{-1*}(\hat{\theta}_3, \hat{\phi}_3) \\ \mathrm{Y}_1^{0*}(\hat{\theta}_1, \hat{\phi}_1) & \mathrm{Y}_1^{0*}(\hat{\theta}_2, \hat{\phi}_2) & \mathrm{Y}_1^{0*}(\hat{\theta}_2, \hat{\phi}_2) \\ \mathrm{Y}_1^{1*}(\hat{\theta}_1, \hat{\phi}_1) & \mathrm{Y}_1^{1*}(\hat{\theta}_2, \hat{\phi}_2) & \mathrm{Y}_1^{1*}(\hat{\theta}_2, \hat{\phi}_2) \end{bmatrix}. \tag{44}$$

Now note that it may be shown that as $K, L \to \infty$, then the matrices $\mathbf{Y}(\mathbf{r}_k)$ and $\mathbf{Y}(\hat{\mathbf{r}}_l)$ become unitary matrices. For example, the diagonal elements of the matrix $\mathbf{Y}^{\mathrm{H}}(\mathbf{r}_k)\mathbf{Y}(\mathbf{r}_k)$ consists of terms given by

$$\mathbf{y}_n^{m\mathrm{H}}(\mathbf{r}_k)\mathbf{y}_n^m(\mathbf{r}_k) = |\mathrm{Y}_n^m(\theta_1, \phi_1)|^2 + |\mathrm{Y}_n^m(\theta_2, \phi_2)|^2 \ldots |\mathrm{Y}_n^m(\theta_K, \phi_K)|^2 = \sum_{k=1}^{K} |\mathrm{Y}_n^m(\theta_k, \phi_k)|^2. \tag{45}$$

The orthogonality property of the spherical harmonics given by equation (9) shows that

$$\int_0^{2\pi} \int_0^{\pi} |\mathrm{Y}_n^m(\theta, \phi)|^2 \sin\theta \, \mathrm{d}\theta \, \mathrm{d}\phi = 1. \tag{46}$$

The term $\sin\theta \, \mathrm{d}\theta \, \mathrm{d}\phi$ can be regarded as an element of area of a sphere of unit radius, and if the K points at which the spherical harmonics are sampled are at the centres of segments of

equal area, the integral in equation (47) can be expressed as the summation

$$\sum_{k=1}^{K} |Y_n^m(\theta, \phi)|^2 \Delta S_k = 1. \tag{47}$$

Since $\Delta S_k = 4\pi/K$, then it follows that the summation in equation (45) will tend to a value of $K/4\pi$ ad $K \to \infty$. By an exactly analogous argument, it is evident that the orthogonality property of the spherical harmonics results in the off-diagonal terms of the matrix $\mathbf{Y}^H(\mathbf{r}_k)\mathbf{Y}(\mathbf{r}_k)$ tending to zero as $K \to \infty$. It is thus concluded that

$$\mathbf{Y}^H(\mathbf{r}_k)\mathbf{Y}(\mathbf{r}_k) = (K/4\pi)\mathbf{I} \quad \text{as } K \to \infty \tag{48}$$

and similarly that

$$\mathbf{Y}^H(\hat{\mathbf{r}}_l)\mathbf{Y}(\hat{\mathbf{r}}_l) = (L/4\pi)\mathbf{I} \quad \text{as } L \to \infty. \tag{49}$$

2.5. THE SINGULAR-VALUE DECOMPOSITION AND THE SPHERICAL HARMONICS

It will be demonstrated by the numerical simulations presented below that there is indeed, under certain circumstances, a direct connection between the results of the singular value decomposition of the Green function matrix and the matrices $\mathbf{Y}(\mathbf{r}_k)$ and $\mathbf{Y}(\hat{\mathbf{r}}_l)$ of sampled spherical harmonics. Specifically, it will be demonstrated that when $\mathbf{Y}(\hat{\mathbf{r}}_l)$ and $\mathbf{Y}(\mathbf{r}_k)$ can be regarded as unitary matrices, such that equations (48) and (49) hold to a good approximation, then one may write

$$\mathbf{U}_N = \mathbf{Y}(\mathbf{r}_k)\mathbf{T}(\mathbf{r}_k), \qquad \mathbf{V}_N = \mathbf{Y}(\hat{\mathbf{r}}_l)\mathbf{T}(\hat{\mathbf{r}}_l). \tag{50a, b}$$

The matrices $\mathbf{U}_N$ and $\mathbf{V}_N$ comprise the left and right singular vectors associated with the first N singular values which, if the SVD is taken of the truncated Green function matrix $\mathbf{G}_N(\mathbf{r}|\hat{\mathbf{r}})$, are the only non-zero singular values. The matrices $\mathbf{U}_N$ and $\mathbf{V}_N$ are found to be linear combinations of the sampled spherical harmonics. The matrices $\mathbf{T}(\mathbf{r}_k)$ and $\mathbf{T}(\hat{\mathbf{r}}_k)$ effectively specify the combinations of the columns of $\mathbf{Y}(\mathbf{r}_k)$ and $\mathbf{Y}(\hat{\mathbf{r}}_l)$, respectively, that must be added to produce the columns of $\mathbf{U}_N$ and $\mathbf{V}_N$. In fact, the left and right singular vectors are found to be linear combinations of sampled spherical harmonics of a certain order n, and this results in the matrices $\mathbf{T}(\mathbf{r}_k)$ and $\mathbf{T}(\hat{\mathbf{r}}_l)$ having a certain block diagonal structure. Furthermore, since $\mathbf{U}_N$ and $\mathbf{V}_N$ are unitary, and when $\mathbf{Y}(\mathbf{r}_k)$ and $\mathbf{Y}(\hat{\mathbf{r}}_l)$ are unitary, then both $\mathbf{T}(\mathbf{r}_k)$ and $\mathbf{T}(\hat{\mathbf{r}}_l)$ must be unitary. This follows since from equations (50a) and (33a)

$$\mathbf{U}_N^H\mathbf{U}_N = \mathbf{T}^H(\mathbf{r}_k)\mathbf{Y}^H(\mathbf{r}_k)\mathbf{Y}(\mathbf{r}_k)\mathbf{T}(\mathbf{r}_k) = \mathbf{I} \tag{51}$$

and when $\mathbf{Y}^H(\mathbf{r}_k)\mathbf{Y}(\mathbf{r}_k) = (K/4\pi)\mathbf{I}$, then it follows that $\mathbf{T}^H(\mathbf{r}_k)\mathbf{T}(\mathbf{r}_k) = (4\pi/K)\mathbf{I}$. Similarly, $\mathbf{T}^H(\hat{\mathbf{r}}_l)\mathbf{T}(\hat{\mathbf{r}}_l) = (4\pi/L)\mathbf{I}$. Thus, it follows from equations (50a, b) that the SVD of the Green function matrix given by equation (31) can be written as

$$\mathbf{G}_N(\mathbf{r}|\hat{\mathbf{r}}) = \mathbf{Y}(\mathbf{r}_k)\mathbf{T}(\mathbf{r}_k)\mathbf{\Sigma}_N\mathbf{T}^H(\hat{\mathbf{r}}_l)\mathbf{Y}^H(\hat{\mathbf{r}}_l), \tag{52}$$

where $\mathbf{\Sigma}_N$ is the diagonal matrix of the N non-zero real singular values. It is also evident from equation (44) therefore that the diagonal matrix $\mathbf{F}$ of the complex amplitudes of the spherical harmonics is given by

$$\mathbf{F} = \mathbf{T}(\mathbf{r}_k)\mathbf{\Sigma}_N\mathbf{T}^H(\hat{\mathbf{r}}_l). \tag{53}$$

These findings are confirmed by the results of the numerical simulations presented below. It will also be shown that for these results to hold, that it is vital that the points on the surface of the sphere and the points on the surrounding spherical surface are sampled at the centres of segments of equal area. This ensures the orthogonality of the columns of the matrices $\mathbf{Y}(\mathbf{r}_h)$ and $\mathbf{Y}(\hat{\mathbf{r}}_l)$.

3. NUMERICAL SIMULATIONS BASED ON THE ANALYTICAL MODEL OF RADIATION FROM A SPHERE

3.1. COMPUTATIONAL MODEL

The Green function given by equation (29) was used in order to construct the matrix of Green functions relating sources placed at 32 points on the surface of a rigid sphere of radius 0·1 m to 32 points on a surrounding farfield spherical surface of radius 10 m. The number of points chosen enabled both spherical surfaces to be divided into 60 segments of equal area as illustrated in Figure 1. A number of terms given by $n = 4$ was used in the spherical harmonic series expansion used in the Green function resulting in a total number of $N = 25$ terms in the series. It was assumed that $\rho_0 c_0 = 411{\cdot}4$ Rayls. The SVD of this matrix was undertaken using the "SVD" routine in MATHEMATICA [21] and yielded only 25 significant singular values σ_i. The number of singular values found was thus equal exactly to the total number of terms in the spherical harmonic expansion (i.e., one term corresponding to $n = 0$, three terms corresponding to $n = 1$, five terms corresponding to $n = 2$, seven terms corresponding to $n = 3$ and so forth). The remaining singular values were smaller than a factor of 10^{-10} times the smallest significant singular value at a value of ka of 0·1. A plot of the variation of the dominant 16 non-zero singular values as a function of ka is shown in Figure 2. It is clear that the singular values are grouped in spherical harmonic order with the largest singular value corresponding to $n = 0$, the next three corresponding to $n = 1$, the next five corresponding to $n = 2$ and the next seven corresponding to $n = 3$. The real part of the singular vector corresponding to $n = 0$, 1 and 2 which are given by the

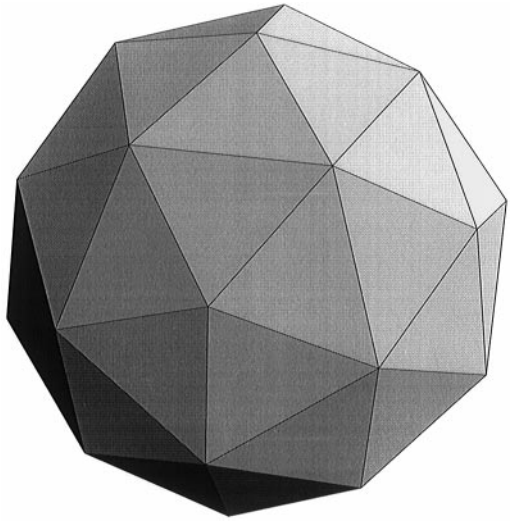

Figure 1. A spherical surface sampled at 32 uniformly distributed points. The points used are at the vertices of the triangular mesh elements.

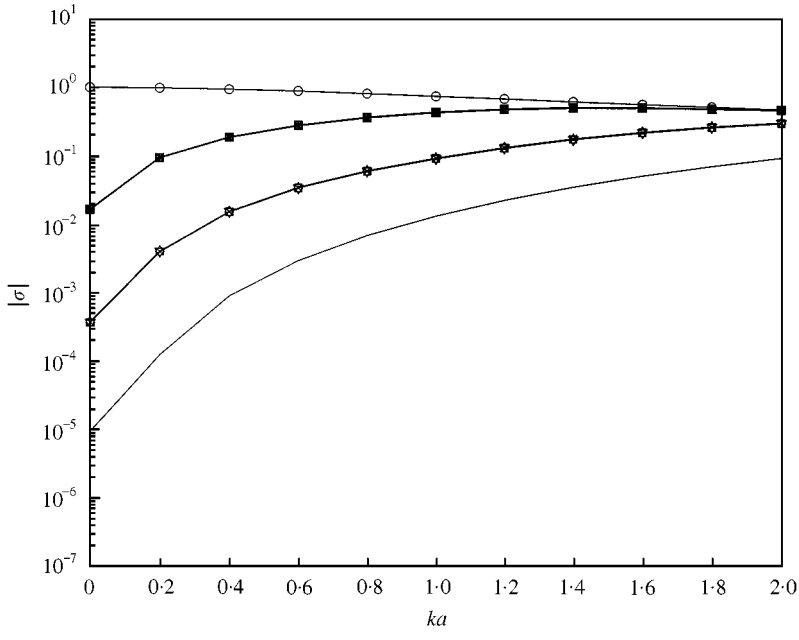

Figure 2. The singular values of the analytically generated 32×32 Green's function matrix relating points on the surface of a rigid sphere of radius a to points on the surface of a farfield surface of radius $100a$. Both spherical surfaces are sampled using the mesh illustrated in Figure 1: —○—, σ_1; —■—, $\sigma_2 \rightarrow \sigma_4$; —☆—, $\sigma_5 \rightarrow \sigma_9$; ——, $\sigma_{10} \rightarrow \sigma_{16}$.

columns $\mathbf{u}_i$ are shown as a surface colour map in Figure 3(a). These plots clearly show the "monopole-like", "dipole-like" and "quadrupole-like" nature of the singular vectors associated, respectively, with spherical harmonic orders corresponding to $n = 0$, 1, 2. (Note however, as discussed in detail by Morse and Ingard [15, see Chapter 7, p. 346], the sound fields associated with the multipole expansion are not simply related to the spherical harmonics; the quadrupole field for example consisting of a combination of spherical harmonics of order $n = 2$ and a monopole field). For comparison, the real and imaginary parts of the spherical harmonics corresponding to $n = 0$, 1 and 2 are shown in Figures 3(b) and 3(c) respectively. Clearly, the spatial patterns involved are very similar to those of the left singular vectors, although the relationships between them are not obvious from the figures.

3.2. CALCULATION OF THE UNITARY TRANSFORMATION MATRICES

A check was undertaken on the unitary nature of the matrices $\mathbf{Y}(\mathbf{r}_k)$ and $\mathbf{Y}(\hat{\mathbf{r}}_l)$ as defined in equation (43) at a value of $ka = 0{\cdot}1$. These matrices of sampled spherical harmonics were found, for the sampling geometry illustrated in Figure 1, to be unitary to an extremely good approximation. The matrices $\mathbf{Y}^{\mathrm{H}}(\mathbf{r}_k)\mathbf{Y}(\mathbf{r}_k)$ and $\mathbf{Y}^{\mathrm{H}}(\hat{\mathbf{r}}_l)\mathbf{Y}(\hat{\mathbf{r}}_l)$ were found to be given by $(K/4\pi)\mathbf{I}$ and $(L/4\pi)\mathbf{I}$, respectively, to a very good accuracy although the maximum diagonal term exceeded the theoretical value by 3·7%. The maximum off-diagonal term was 3% of the theoretical value of the diagonal terms. The elements of the matrix $\mathbf{Y}^{\mathrm{H}}(\mathbf{r}_k)\mathbf{Y}(\mathbf{r}_k)$ are shown on a grey-scale plot in Figure 4. It is interesting to note, however, that the sum of the diagonal terms in these matrices was *exactly* equal to the theoretical value. Similarly, the sum of the off-diagonal terms was a factor 10^{-5} smaller than the theoretical value of the diagonal terms.

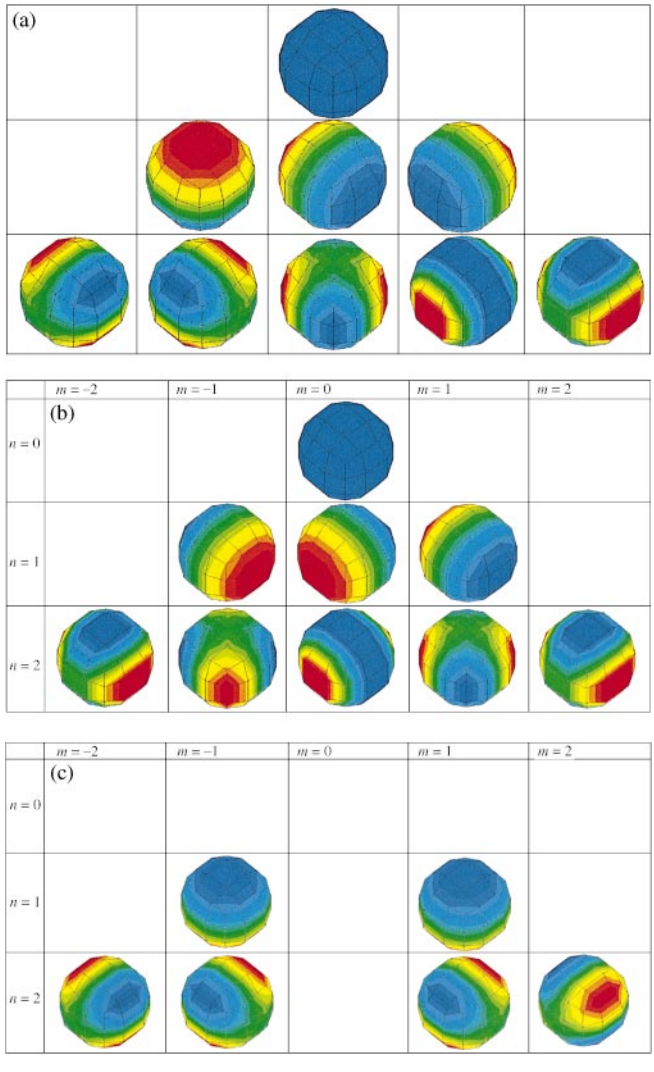

Figure 3. Three-dimensional colour maps illustrating (a) the variation over the farfield sphere of the real part of the left singular vectors of the analytically generated 32×32 Green's function matrix (the plots shown correspond to the nine most dominant singular values), (b) the real part of the spherical harmonics evaluated over the same spherical surface, (c) the corresponding imaginary parts of the spherical harmonics. The values in each row were normalized to ± 1: $+1$ red, -1 blue.

The matrices $\mathbf{T}(\mathbf{r}_k)$ and $\mathbf{T}(\hat{\mathbf{r}}_l)$ were then calculated. Since there were only $n = 4$ terms in the spherical harmonic series expansion and thus only 16 non-zero singular values, only the first $N = 16$ columns of the matrices $\mathbf{U}$ and $\mathbf{V}$ were used in SVD expansion of the matrix $\mathbf{G}_N(\mathbf{r}\,|\,\hat{\mathbf{r}})$. Thus,

$$\mathbf{G}_N(\mathbf{r}\,|\,\hat{\mathbf{r}}) = \mathbf{U}_N \boldsymbol{\Sigma}_N \mathbf{V}_N^{\mathrm{H}} \tag{54}$$

and the unitary transformation matrices are defined using equations (50a, b). Pre-multiplication of these equations, respectively, by $\mathbf{Y}^{\mathrm{H}}(\mathbf{r}_k)$ and $\mathbf{Y}^{\mathrm{H}}(\hat{\mathbf{r}}_l)$ then shows that

$$\mathbf{T}(\mathbf{r}_k) = (4\pi/K)\mathbf{Y}^{\mathrm{H}}(\mathbf{r}_k)\mathbf{U}_N, \qquad \mathbf{T}(\hat{\mathbf{r}}_l) = (4\pi/L)\mathbf{Y}^{\mathrm{H}}(\hat{\mathbf{r}}_l)\mathbf{V}_N. \tag{55a, b}$$

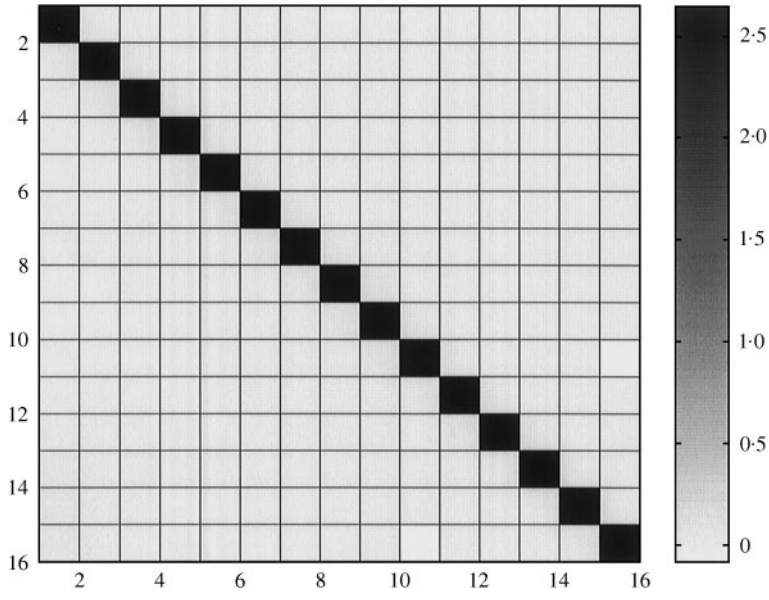

Figure 4. A grey-scale plot of the values of the real parts of the elements of the matrix $\mathbf{Y}(\mathbf{r}_k)^{\mathrm{H}}\mathbf{Y}(\mathbf{r}_k)$, where the values of $\mathbf{r}_k$ chosen correspond to 32 uniformly distributed points on the sphere.

The results of these computations are shown in Figures 5 and 6 which show both the real and imaginary parts of these two matrices and their block diagonal structure. Note that the blocks of terms in these matrices are arranged in accordance with spherical harmonic order n, with submatrices of dimension 1×1, 3×3, 5×5 and 7×7 appearing in diagonal blocks. This in turn implies that the first left and right singular vectors are equal to the first columns of the matrices $\mathbf{Y}(\mathbf{r}_k)$ and $\mathbf{Y}(\hat{\mathbf{r}}_l)$, respectively (i.e., corresponding to the $n = 0$ spherical harmonic), whilst the second, third and fourth singular vectors are linear combinations of the second, third and fourth columns of $\mathbf{Y}(\mathbf{r}_k)$ and $\mathbf{Y}(\hat{\mathbf{r}}_l)$ corresponding to the $n = 1$ spherical harmonics, and so forth. A plot of the elements of the matrix $\mathbf{T}(\mathbf{r}_k)^{\mathrm{H}}\mathbf{T}(\mathbf{r}_k)$ is shown in Figure 7 which confirms the unitary structure of the matrix $\mathbf{T}(\mathbf{r}_k)$.

Finally, a check was undertaken to ensure that the matrix $\mathbf{\Sigma}_N$ of singular values was related to the matrix $\mathbf{F}$ of complex spherical harmonic amplitudes through the relationship $\mathbf{F} = \mathbf{T}(\mathbf{r}_k)\mathbf{\Sigma}_N\mathbf{T}^{\mathrm{H}}(\hat{\mathbf{r}}_l)$. It was found that this relationship holds to an excellent approximation. Figure 8 shows on a logarithmic scale the elements of $\mathrm{Re}\{\mathbf{T}(\mathbf{r}_k)\mathbf{\Sigma}_N\mathbf{T}^{\mathrm{H}}(\mathbf{r}_l)\}$ computed from this expression. The results are in agreement with those deduced from the analytical solution to within the precision of the numerical calculation.

3.2. SENSITIVITY TO CHOICE OF MESH

A further set of numerical simulations were undertaken that were based on the above analytical model, but with non-uniformly sampled spherical surfaces. The surface mesh used is illustrated in Figure 9. This form of sampling was applied both on the surface of the rigid sphere and on the farfield surface. In this case, the matrices $\mathbf{Y}(\mathbf{r}_k)$ and $\mathbf{Y}(\hat{\mathbf{r}}_l)$ were no longer found to be unitary. A plot showing the real part of $\mathbf{Y}^{\mathrm{H}}(\mathbf{r}_k)\mathbf{Y}(\mathbf{r}_k)$ is shown in Figure 10 which demonstrates that although the diagonal terms are still dominant, the diagonal terms are a maximum of 19·1% above the theoretical value, although their sum is again exactly equal

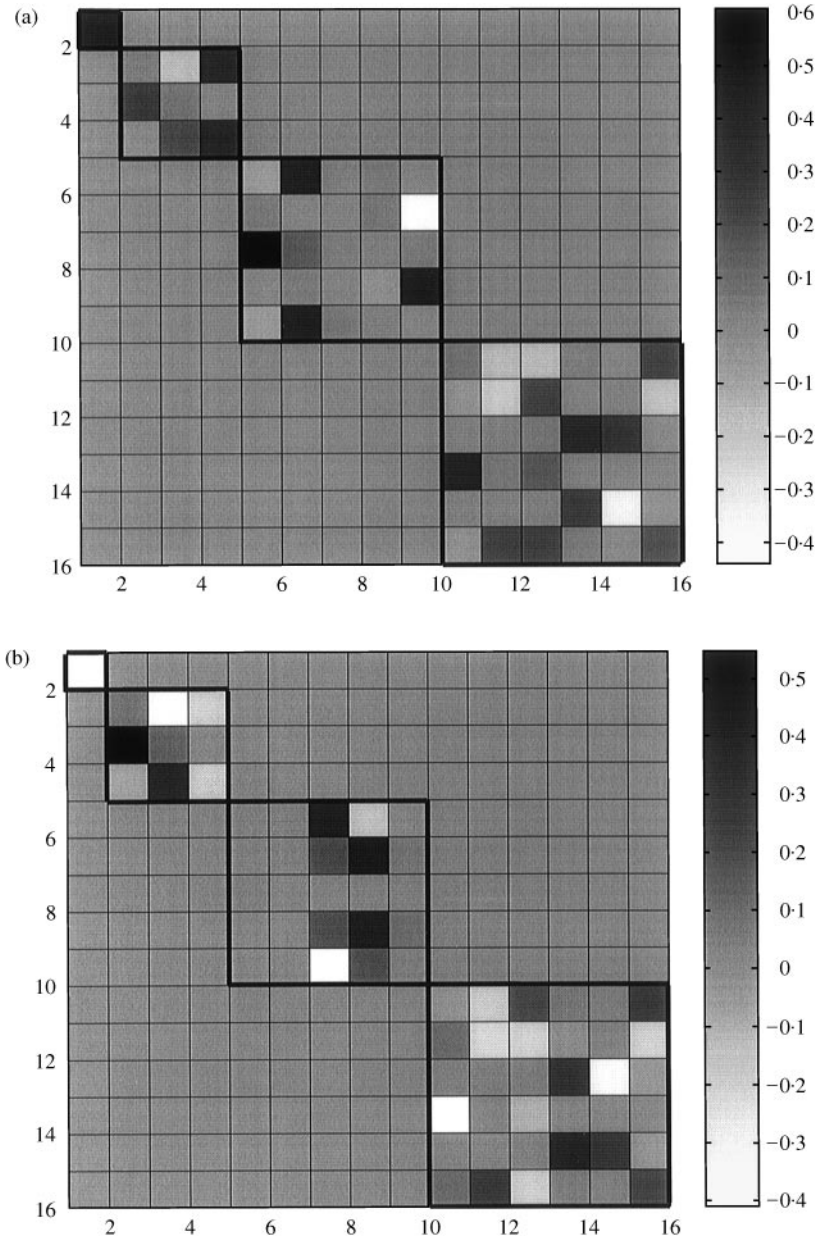

Figure 5. A grey-scale plot of the (a) real and (b) imaginary parts of the elements of the matrix $\mathbf{T}(\mathbf{r}_k)$ associated with the analytically generated 32×32 Green's function matrix.

to the theoretical value. The off-diagonal terms are a maximum of 24·7% of the theoretically predicted diagonal terms. However, the *sum* of the off diagonal terms was 0·05% of the theoretically predicted values of the diagonal terms. Similarly, plots of the real and imaginary parts of $\mathbf{T}(\mathbf{r}_k)$ for this case are shown in Figure 11 and a plot of the real part of $\mathbf{T}(\mathbf{r}_k)^{\mathrm{H}}\mathbf{T}(\mathbf{r}_k)$ is shown in Figure 12. Also a plot of the real part of the matrix product $\mathbf{T}(\mathbf{r}_k)\mathbf{\Sigma}_N\mathbf{T}^{\mathrm{H}}(\hat{\mathbf{r}}_l)$ is shown in Figure 13. In this case, the agreement with the results for the analytical solution for $\mathrm{Re}\{\mathbf{F}\}$ is far less good.

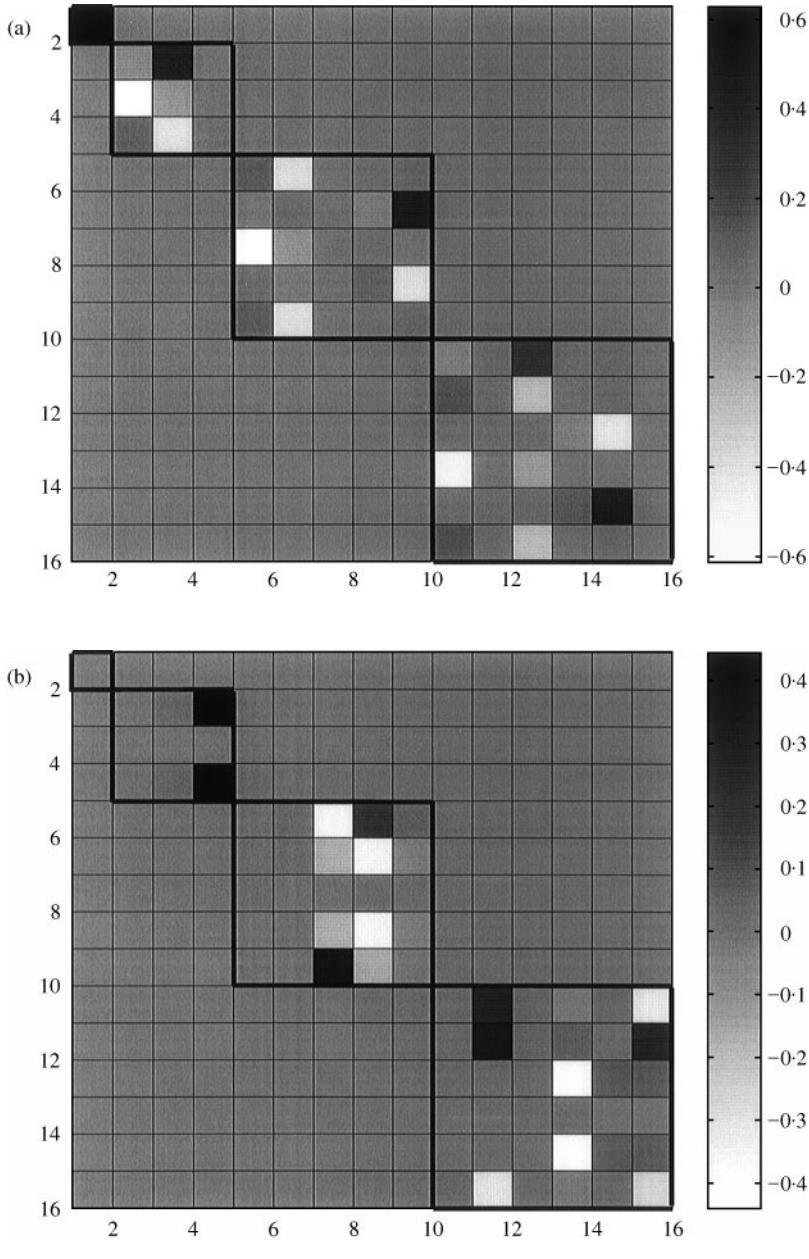

Figure 6. A grey-scale plot of the (a) real and (b) imaginary parts of the elements of the matrix $\mathbf{T}(\hat{\mathbf{r}}_l)$ associated with the analytically generated 32×32 Green's function matrix.

A plot of the 20 dominant singular values is shown in this case as a function of ka in Figure 14. Again $n = 4$ terms were used in the spherical harmonic series and 25 dominant singular values were yielded by the SVD. The smallest singular values were again found to be a factor 10^{-9} times the smallest dominant singular value. However, it is clear that the singular values are no longer grouped in spherical harmonic order as convincingly as the

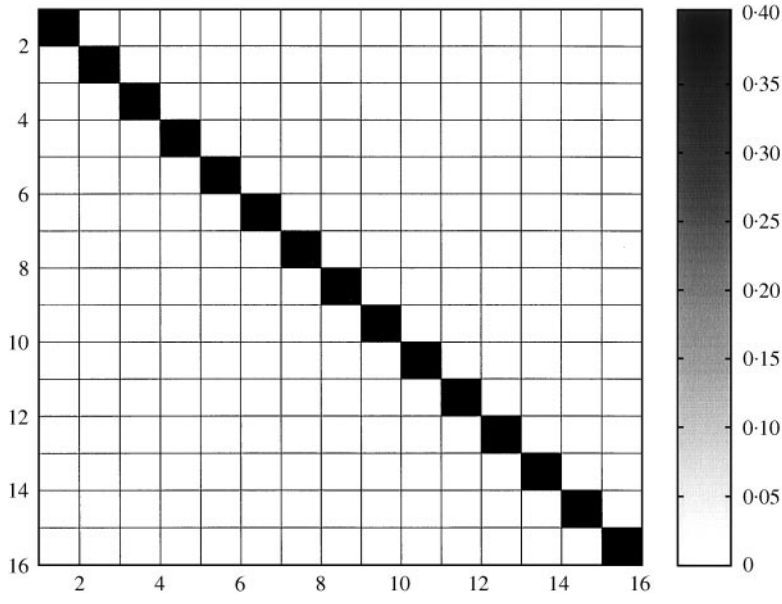

Figure 7. A grey-scale plot of the real parts of the elements of the matrix $\mathbf{T}(\mathbf{r}_k)^{\mathrm{H}}\mathbf{T}(\mathbf{r}_k)$ associated with the analytically generated 32×32 Green's function matrix.

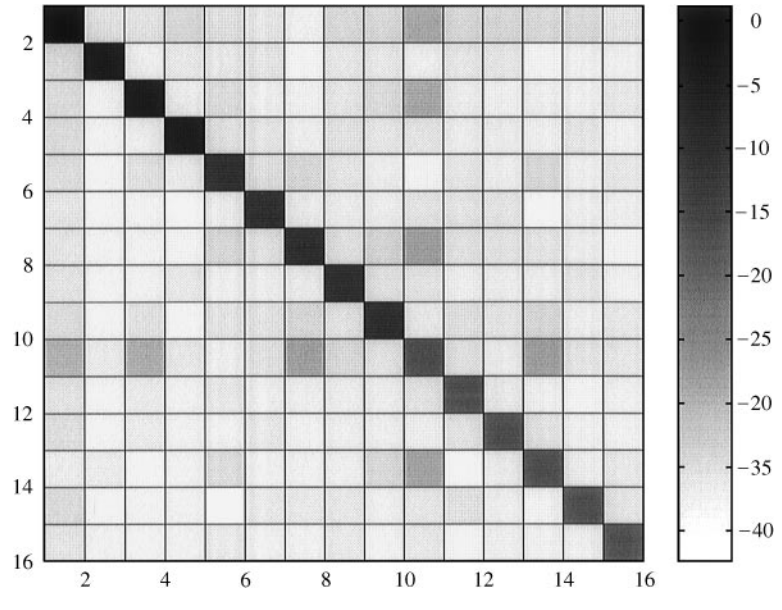

Figure 8. A grey-scale plot (on a logarithmic scale) of the real parts of the elements of the matrix $\mathbf{T}(\mathbf{r}_k)\boldsymbol{\Sigma}_N\mathbf{T}(\hat{\mathbf{r}}_l)^{\mathrm{H}}$ associated with the 32×32 analytically generated Green's function matrix.

case with perfectly uniform sampling of the field. This therefore illustrates the sensitivity of the choice of mesh to the relationship between the "source modes" and "field modes" comprising the columns of **V** and **U** and which is quantified by the relevant singular value.

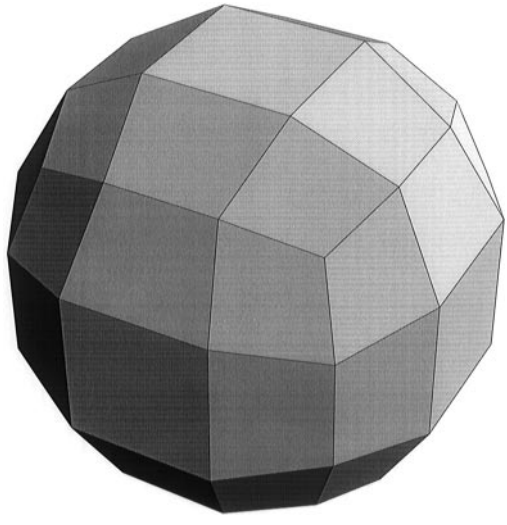

Figure 9. A spherical surface sampled with an approximately uniform distribution of 56 points. The points used are at the vertices of the quadrilateral mesh elements.

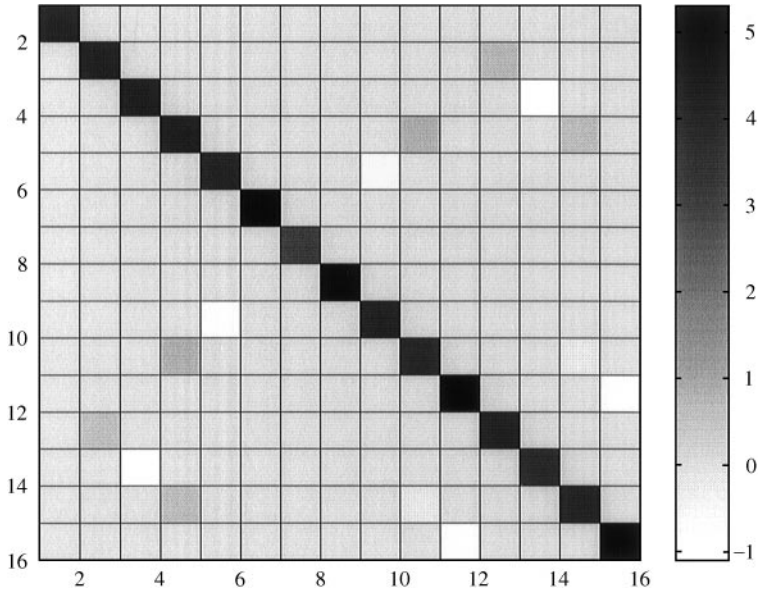

Figure 10. A grey-scale plot of the values of the real parts of the elements of the matrix $\mathbf{Y}(\mathbf{r}_k)^{\mathrm{H}}\mathbf{Y}(\mathbf{r}_k)$ where the values of $\mathbf{r}_k$ chosen correspond to 56 points distributed on the far field of a sphere in the manner illustrated in Figure 9.

4. NUMERICAL SIMULATION BASED ON THE BOUNDARY ELEMENT METHOD

4.1. BOUNDARY ELEMENT SOFTWARE

The numerical simulations undertaken below were undertaken using the SYSNOISE software package [22] which uses the boundary element method in order to compute numerically the solution of the homogeneous Helmholtz equation. This is given by equation

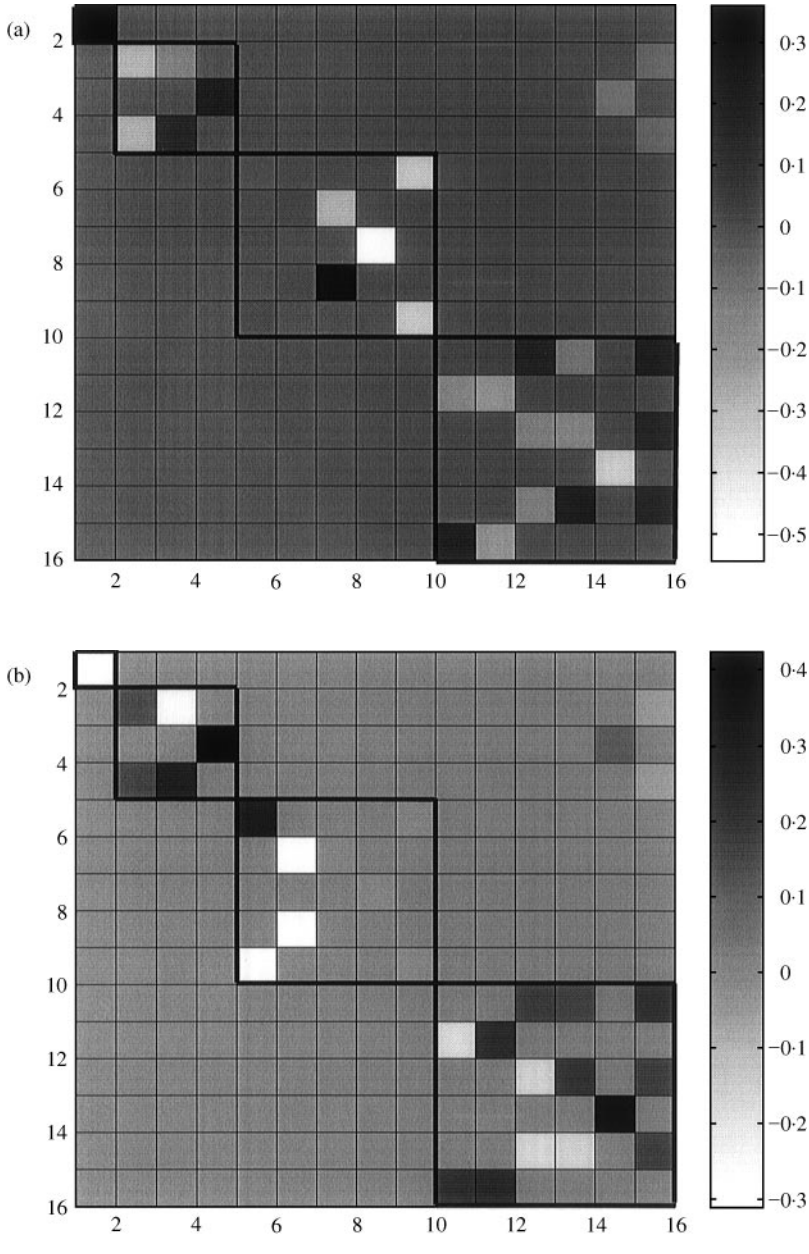

Figure 11. A grey-scale plot of the (a) real and (b) imaginary parts of the elements of the matrix $\mathbf{T}(\mathbf{r}_k)$ associated with the analytically generated 56×56 Green's function matrix.

(22) which when using the free-space Green function $g(\mathbf{r}\,|\,\mathbf{r}_0)$ reduces to

$$p(\mathbf{r}) = \int_S [g(\mathbf{r}\,|\,\mathbf{r}_0)\nabla_0 p(\mathbf{r}_0) - p(\mathbf{r}_0)\nabla_0 g(\mathbf{r}\,|\,\mathbf{r}_0)]\,.\mathbf{n}\,\mathrm{d}S \tag{56}$$

which is the Kirchhoff–Helmholtz integral equation. SYSNOISE first solves the integral equation for the surface pressure $p(\mathbf{r}_0)$. Full details are given in reference [22].

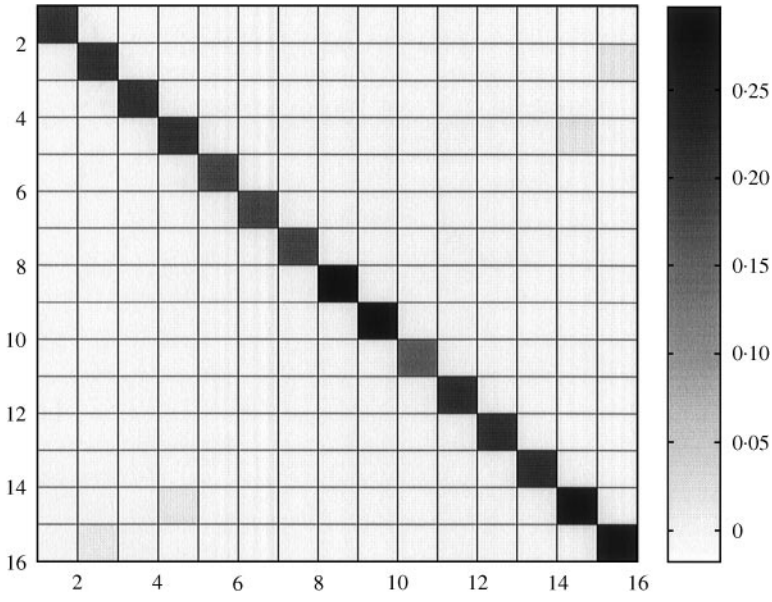

Figure 12. A grey-scale plot of the real parts of the elements of the matrix $\mathbf{T}(\mathbf{r}_k)^{\mathrm{H}}\mathbf{T}(\mathbf{r}_k)$ associated with the analytically generated 56×56 Green's function matrix.

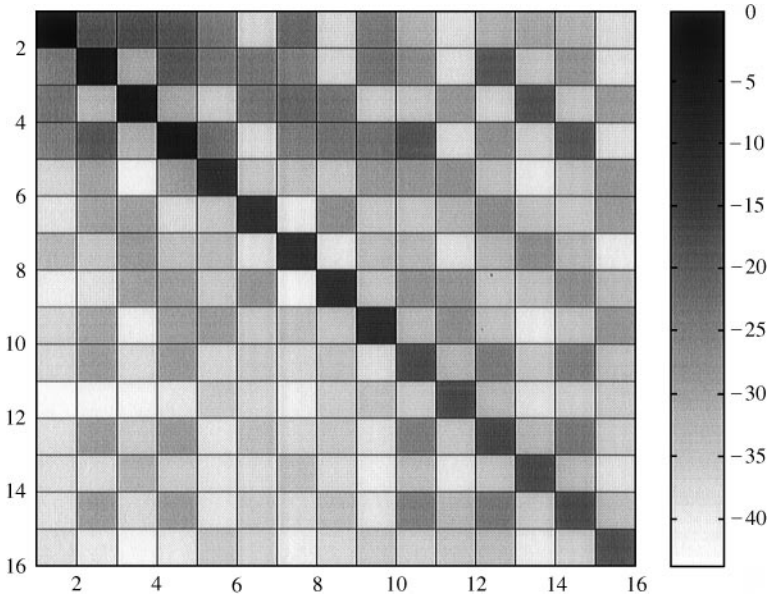

Figure 13. A grey-scale plot (on a logarithmic scale) of the real parts of the elements of the matrix $\mathbf{T}(\mathbf{r}_k)\mathbf{\Sigma}_N\mathbf{T}(\hat{\mathbf{r}}_l)^{\mathrm{H}}$ associated with the analytically generated 56×56 Green's function matrix.

As an initial verification of the software, a numerical solution was computed for the case of the sphere whose surface was sampled as illustrated in Figure 15. The SVD of the resulting Green function matrix was then undertaken and calculated using MATLAB [23]. The results are illustrated in Figure 16. The agreement with the results for the

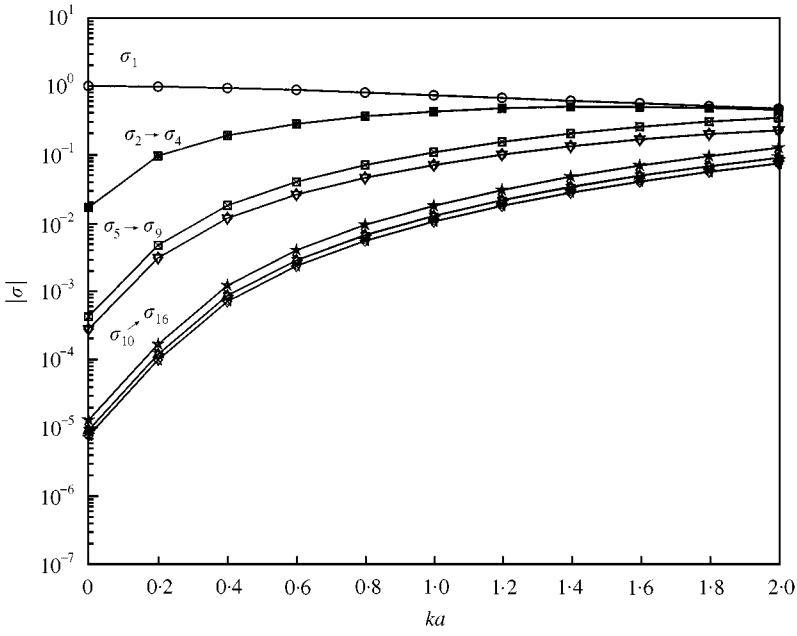

Figure 14. The singular values of the analytically generated 56×56 Green's function matrix relating points on the surface of a rigid sphere of radius a to points on the surface of a far field surface of radius $100a$. Both spherical surfaces were sampled using the mesh illustrated in Figure 9.

sphere sampled as shown in Figure 9 was found to be excellent (compare Figure 16 with Figure 14).

4.2. THE SOURCE AND FIELD MODE SHAPES OF AN ELLIPSOID

As a further illustration of the utility of the SVD in analyzing numerical solutions, another numerical simulation was undertaken using SYSNOISE in order to deduce the "field mode shapes" and "source mode shapes" associated with an ellipsoid and a farfield spherical surface. The ellipsoidal geometry illustrated in Figure 17 was used and the farfield sphere was sampled using the same geometry as that illustrated in Figure 5. Although not shown here, the mode shapes associated with both source and field were very similar to those computed in the case of a sphere, with essentially the same groups of patterns appearing in the left and right singular vectors. However, as illustrated more clearly by the behaviour of the singular values shown in Figure 18, there were subtle departures from the behaviour seen in the case of a sphere. Most notably, the groups of spherical harmonic orders become more spread as the individual singular values depart more from the frequency dependence found with the sphere. In view of the evident sensitivity of the results shown above to the choice of mesh, it is difficult at this stage to be sure to what extent the basic change of geometry influences the results of the SVD. These uncertainties clearly warrant further investigation.

4.3. THE SOURCE AND FIELD MODE SHAPES OF A BAFFLED PINNA

As a final illustration of the great potential of the SVD for analyzing acoustic scattering problems, numerical simulations were undertaken using SYSNOISE in order to deduce the

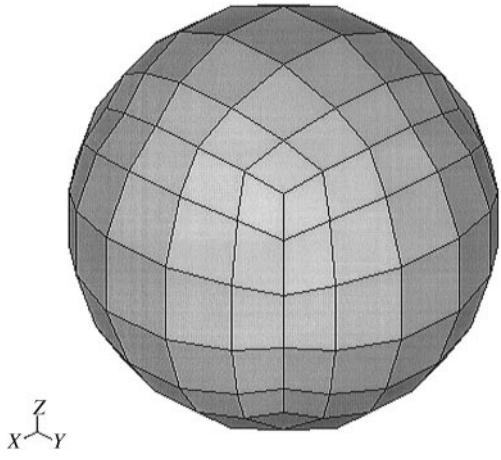

Figure 15. A spherical surface sampled at 152 approximately uniformly distributed points. The points used are at the vertices of the quadrilateral elements.

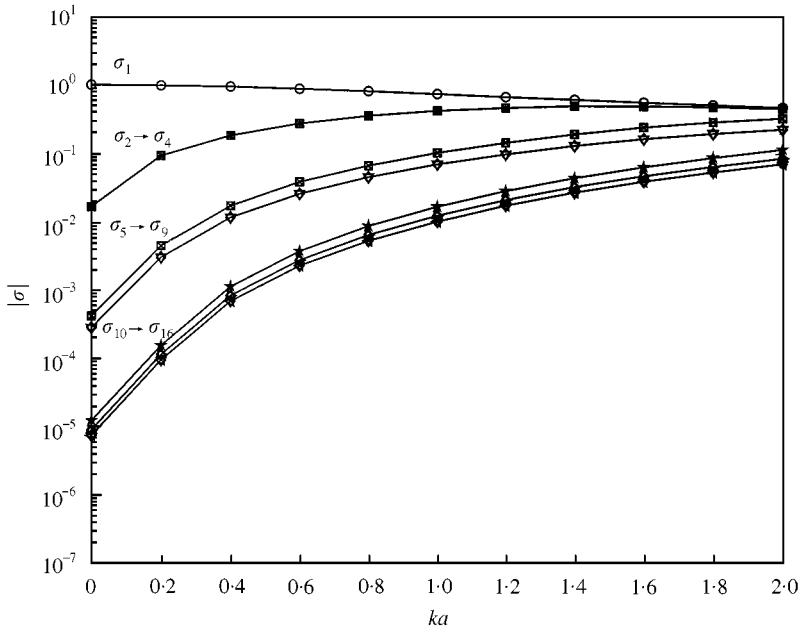

Figure 16. The singular values of the numerically generated 152×152 Green's function matrix relating points on the surface of a rigid sphere of radius a to points on a farfield spherical surface of radius $100a$. Both spherical surfaces were sampled using the mesh illustrated in Figure 15.

matrix of Green functions relating a number of points on the surface of an outer ear (pinna) mounted on an infinite rigid baffle and a number of points on a surrounding farfield hemispherical surface. The pinna chosen was the DB60 pinna associated with the KEMAR dummy head [24]. The computational mesh used was generated by a laser scanning technique first employed for this purpose by Katz [25] and described in detail by Kahana [26]. The mesh used in the computation consisted of 2825 nodes whilst the farfield hemisphere was sampled by using 209 nodes.

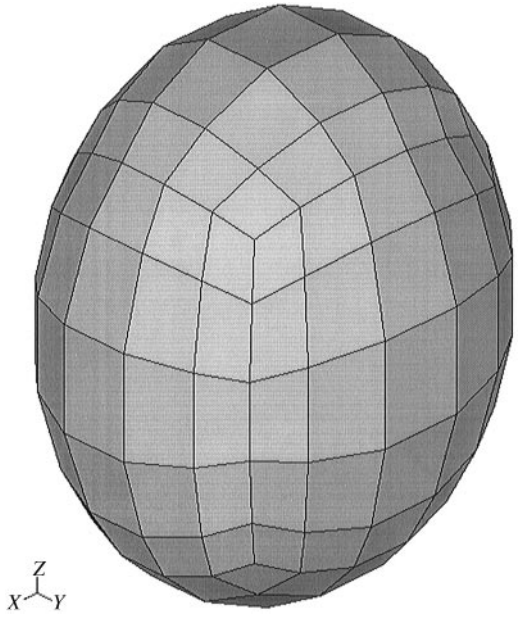

Figure 17. An ellipsoidal surface sampled at 152 approximately uniformly distributed points. The points used are at the vertices of the quadrilateral elements. The ellipsoid has semi-axes of dimensions $a_x = 9{\cdot}6$ cm, $a_y = 7{\cdot}9$ cm, $a_z = 11{\cdot}6$ cm.

The SVD of the resulting Green function matrix was undertaken at a number of discrete frequencies between 2 and 15 kHz. The frequency dependence of the resulting singular values is illustrated in Figure 19. This highlights the behaviour of the first three dominant singular values and also shows the frequency dependence of the next seven largest singular values. The most significant feature of these results is the manner in which the dominant singular value exhibits peaks in amplitude at certain frequencies. It has been found that the corresponding left and right singular vectors also exhibit distinctive spatial patterns at these frequencies.

Figure 20(a) illustrates the real and imaginary parts of the left and right singular vectors associated with the dominant singular value at the frequency of 4600 Hz which is the left-most peak frequency in Figure 19. This peak in the coupling between the field in the region of the pinna and points in the far field appears to be related to the "concha resonance' identified in previous studies [17] of the outer ear response. Although not as sharp as the peak of 4600 Hz, the dominant singular value exhibits a broader peak of lower amplitude centred at about 8800 Hz. Figure 20(b) shows the "mode shape" associated with the pinna at this frequency. This appears to involve a dipole-like response, with the dipole axis in the vertical direction and involving oscillatory flow between the concha and the antihelix. The next sharp peak at 10 300 Hz has the associated mode shapes illustrated in Figure 20(c). This appears to be linked to a longitudinal quadrupole-like response in the vertical direction and appears to involve oscillatory flow between the concha, antihelix and fossa of helix. It should also be noted that the next dominant singular value (σ_2) also has a peak close to their frequency. This mode shape is illustrated in Figure 20(d) and is again dipole-like with a horizontal axis and involves oscillating flow. Finally, the right-most peak occurring in Figure 19 is at about 13 800 Hz and appears to involve a quadrupole-like motion which consists of both a horizontal dipole within the concha and vertical dipole. These mode shapes are shown in Figure 20(e).

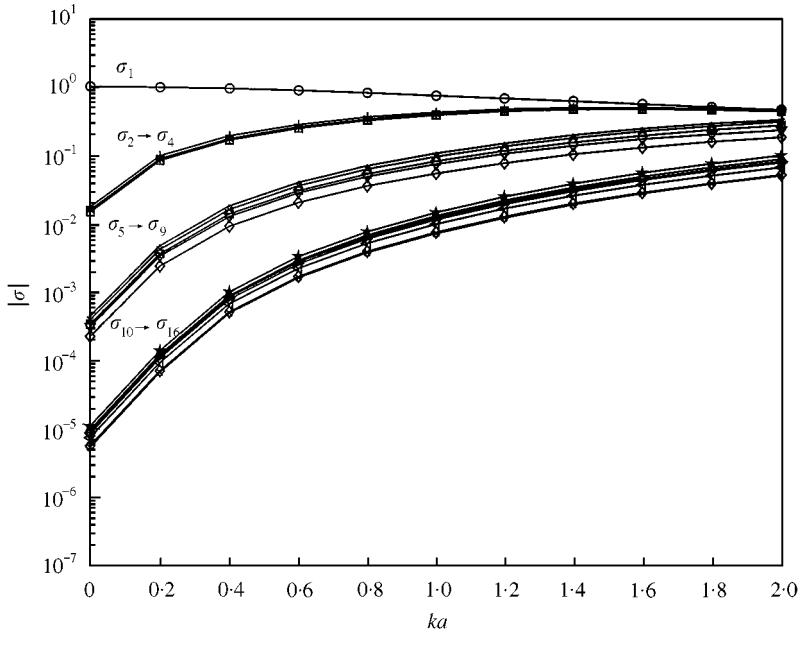

Figure 18. The singular values of numerically generated 152×152 Green's function matrix relating points on the surface of a rigid ellipsoid (distributed as shown in Figure 17) to points on the surface of a farfield sphere of radius $104a_x$ (distributed as shown in Figure 15).

5. DISCUSSION

It is evident from the results presented above that the SVD provides an extremely useful tool for the analysis of the results of numerical analyses of acoustical problems. The clear connection has been made between the classical methods of acoustics which use a series of orthogonal basis functions for describing the spatial characteristics of a sound field and the results of the SVD. In the case of the uniformly sampled spheres, the left and right singular vectors were found to be related to the spherical harmonics by a unitary transformation. It is worth pointing out that both Borgiotti [1] and Photiadis [2] identified the right singular vectors as being closely related to the spherical harmonics used in describing the source distribution. This identification was made by both authors in noting that the total power radiated could be expressed in a certain diagonal form. Photiadis [2] for example, pointed out that "up to a phase, the source and radiation modes are the spherical harmonics". In the context of the work presented here, the total acoustic power radiated to the far field can be expressed as

$$W = \sum_{k=1}^{K} \frac{|p(\mathbf{r}_k)|^2}{2\rho_0 c_0} \Delta S = \frac{\Delta S}{2\rho_0 c_0} \mathbf{p}^{\mathrm{H}}(\mathbf{r}_k)\mathbf{p}(\mathbf{r}_k), \tag{57}$$

where ΔS represents the area of equal area segments with which the far field is sampled. Substitution of the expression for the Green function matrix represented in terms of N spherical harmonics then shows that

$$W \approx \frac{\Delta S}{2\rho_0 c_0} \mathbf{q}^{\mathrm{H}}(\hat{\mathbf{r}}_l)\mathbf{V}_N \boldsymbol{\Sigma}_N^{\mathrm{H}} \boldsymbol{\Sigma}_N \mathbf{V}_N^{\mathrm{H}} \mathbf{q}(\hat{\mathbf{r}}_l). \tag{58}$$

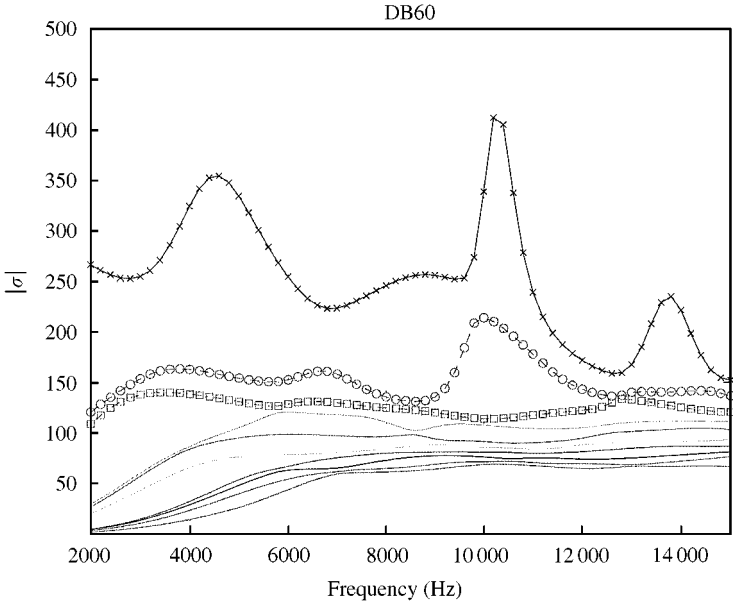

Figure 19. The singular values of the numerically generated 2825×209 Green's function matrix relating 2825 points on the surface of the DB60 KEMAR pinna mounted on a rigid baffle to 209 points distributed approximately uniformly on a farfield hemisphere of radius 3 cm. The calculation is undertaken at 66 frequencies. —×—×—, σ_1; ○⊖○, σ_2; □⊟□, σ_3. The next seven largest singular values are shown unlabelled.

Since $\mathbf{V}_N = \mathbf{Y}(\hat{\mathbf{r}}_l)\mathbf{T}(\hat{\mathbf{r}}_l)$ and since $\mathbf{F} = \mathbf{T}(\mathbf{r}_k)\mathbf{\Sigma}_N\mathbf{T}^{\mathrm{H}}(\hat{\mathbf{r}}_l)$, it is readily shown that this expression can also be written as

$$W \approx (\Delta S/2\rho_0 c_0)\,(L/4\pi)\,\mathbf{q}^{\mathrm{H}}(\hat{\mathbf{r}}_l)\mathbf{Y}(\hat{\mathbf{r}}_l)\mathbf{F}^{\mathrm{H}}\mathbf{F}\mathbf{Y}^{\mathrm{H}}(\hat{\mathbf{r}}_l)\mathbf{q}(\hat{\mathbf{r}}_l). \tag{59}$$

Comparison of equations (58) and (59) thus shows that it is tempting to identify the diagonal matrix of squared singular values $\mathbf{\Sigma}_N^{\mathrm{H}}\mathbf{\Sigma}_N$ with the diagonal matrix of squared terms given by $\mathbf{F}^{\mathrm{H}}\mathbf{F}$. Similarly, it is natural to identify the matrix $\mathbf{V}_N$ of right singular vectors with the matrix of sampled spherical harmonics given by $\mathbf{Y}(\hat{\mathbf{r}}_l)$. The analysis presented above shows that this is not quite the case, in view of the existence of the unitary transformation. Nevertheless, the essential physical principles described by both Borgiotti and Photiadis remain valid and in fact the existence of the unitary transformation can be anticipated directly from the results derived by these authors.

It should be also noted, however, that the spherical harmonic series enables the sound field in the case of uniformly sampled spheres to be described in terms of *frequency-independent* spatial basis functions. Thus, the expression for the Green function given by equation (29), for example, encapsulates the frequency dependence of the sound radiation process within the terms $\mathrm{h}_n^{(2)}(kr)/\mathrm{h}_n^{(2)}(ka)$ which clearly do not have a dependence on θ and ϕ. It is therefore possible, for example, to calculate the time domain response of the system through Fourier transformation of these terms and yet still describe the system response spatially within the series of spherical harmonics. It is not clear that this is possible when using the basis functions provided by the SVD for an arbitrary geometry. The frequency dependence of these basis functions is a matter of current investigation.

Turning to the analysis of the numerically computed results for the baffled pinna, these appear to be highly plausible and in reasonable agreement with the previously measured acoustical characteristic of the outer ear [17–19]. Thus, for example, Shaw [17] suggests

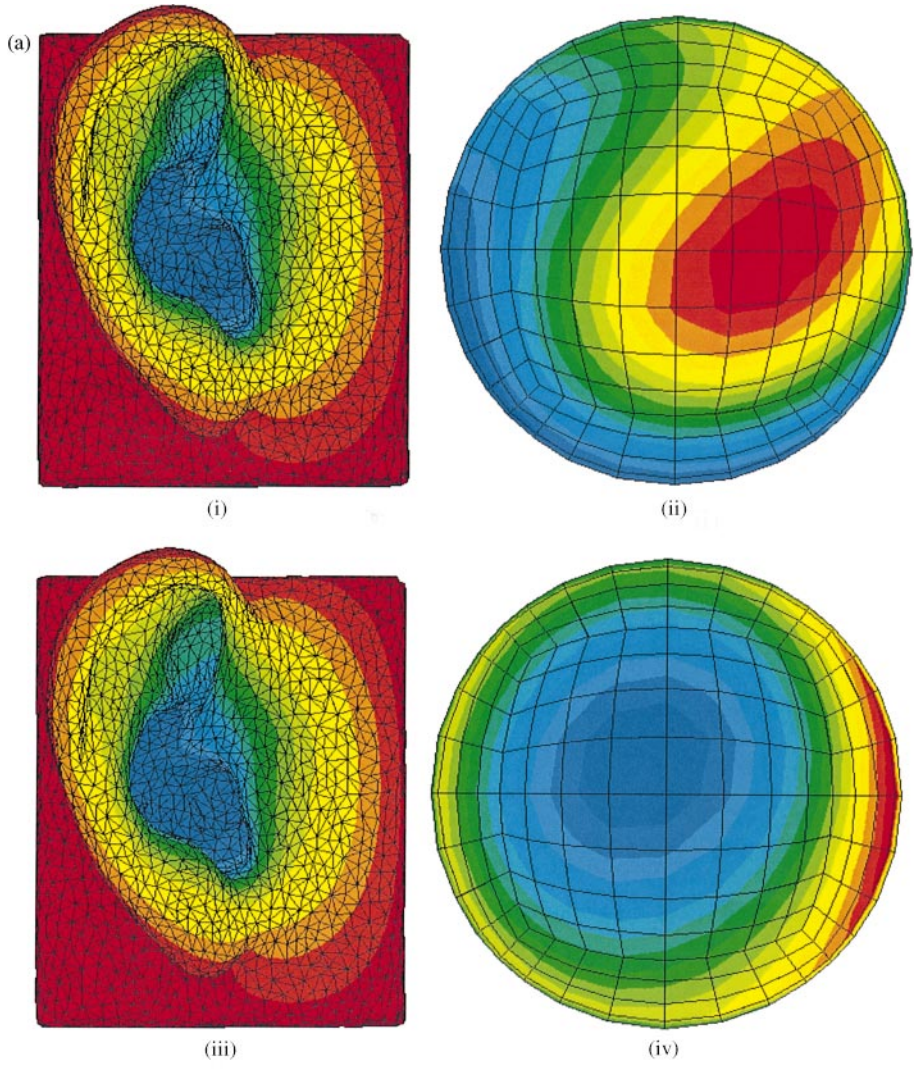

4600 Hz	Minimum scale (blue)	Maximum scale (red)
(i) Real (v)	−4·819e−02	5·574e−03
(ii) Real (u)	−1·352e−02	1·001e−03
(iii) Imag (v)	−1·34e−02	8·906e−02
(iv) Imag (u)	−3·856e−02	1·219e−01

Figure 20. The (i) real (ii) imaginary parts of the right singular vectors and (iii) real (iv) imaginary parts of the left singular vectors associated with the dominant singular values of the numerically generated 2825×209 Green's function matrix for the DB60 KEMAR pinna at (a) 4800 Hz [σ_1], (b) 8800 Hz [σ_1], (c) 10300 Hz [σ_1], (d) 10300 Hz [σ_1], (e) 13800 Hz [σ_1].

that there is a "unidirectional" resonance of the concha at a frequency which, on average, is about 4200 Hz. The dominant singular value for the DB60 pinna analyzed above has a peak at about 4600 Hz which indeed corresponds to a basis function of the pinna which includes a uniform response of the concha (see Figure 20(a)). However, from the associated basis function evaluated on the surrounding farfield hemisphere, there would appear to be at least some directionality associated with this response.

(b)

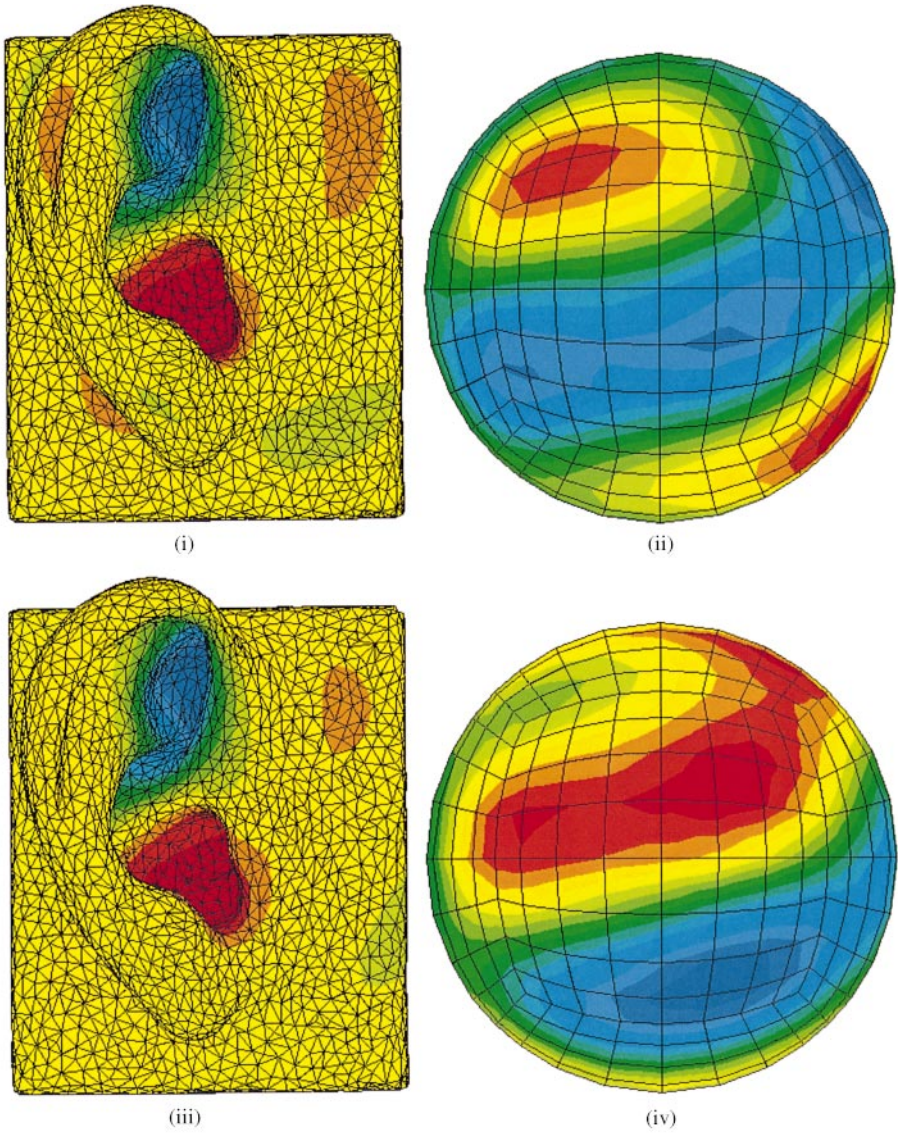

8800 Hz	Minimum scale (blue)	Maximum scale (red)
(i) Real (v)	−6·261e−02	2·274e−02
(ii) Real (u)	−9·497e−02	1·038e−01
(iii) Imag (v)	−5·754e−02	2·099e−02
(iv) Imag (u)	−1·148e−01	9·556e−02

Figure 20. continued

Similarly, Shaw [17] suggests that there is a strong "vertical" dipole-like resonance on average at about 7100 Hz and this is indeed exhibited clearly by the results shown in Figure 20(b) for the dominant basis functions at 8800 Hz. However, in this case, the dipole-like motion appears to involve not only the concha but a combination of the concha and the antihelix. The corresponding farfield basis functions also show a predominant directivity in the vertical direction. Shaw suggests that the third mode consists of

(c)

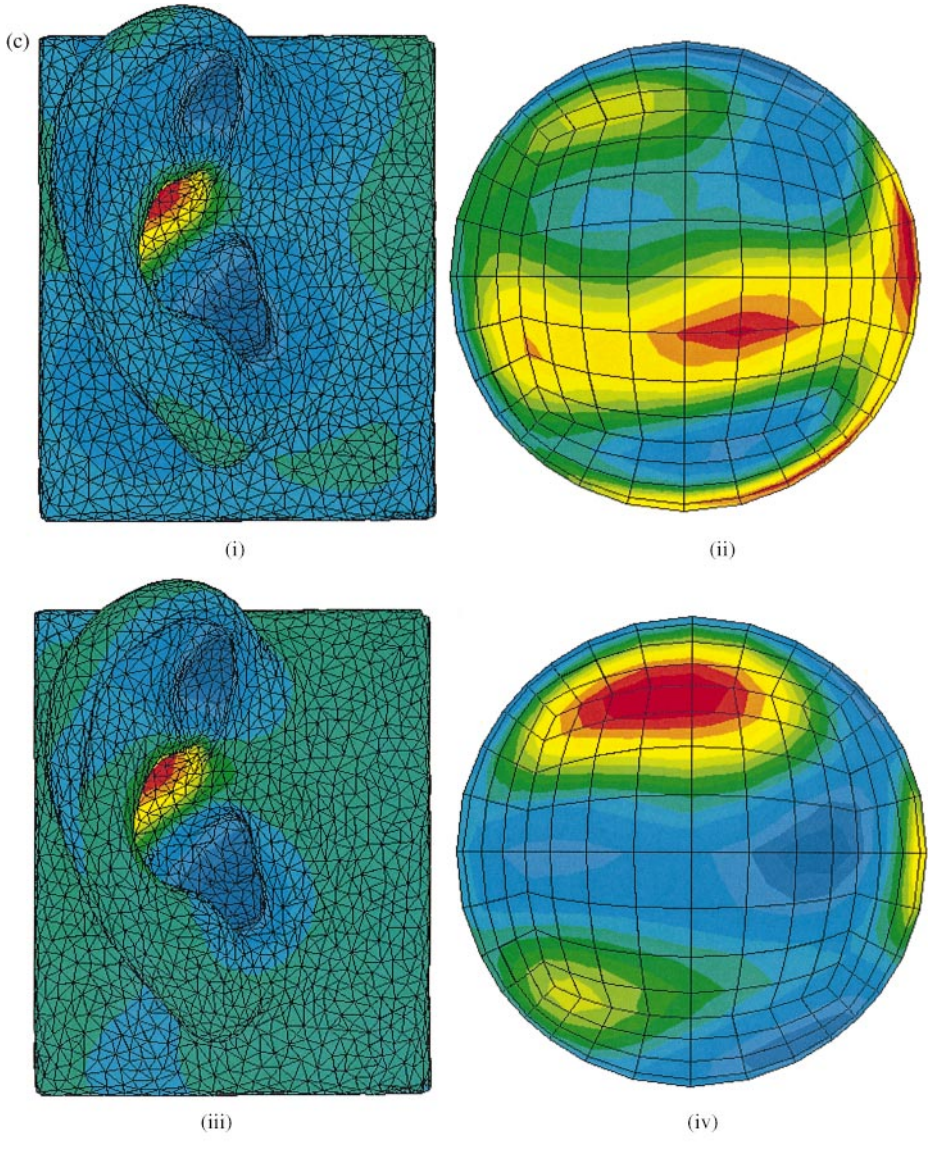

(i) (ii)

(iii) (iv)

10 300 Hz/σ_1	Minimum scale (blue)	Maximum scale (red)
(i) Real (v)	−1·097e−02	2·132e−02
(ii) Real (u)	−1·044e−01	1·181e−01
(iii) Imag (v)	−5·23e−02	8·325e−02
(iv) Imag (u)	−7·89e−02	1·409e−01

Figure 20. continued

a “horizontal” dipole-like resonance at about 9600 Hz on average and indeed a horizontal dipole is observed in the numerical results for the second-most dominant singular value at 10 300 Hz (see Figure 20(c)). The dominant singular value at this frequency however (see Figure 20(d)) exhibits a basis function which is more akin to a vertically oriented longitudinal quadrupole. Finally, the results presented here suggest that the next most significant mode is quadrupole-like and at a frequency of 13 800 Hz (Shaw observed more

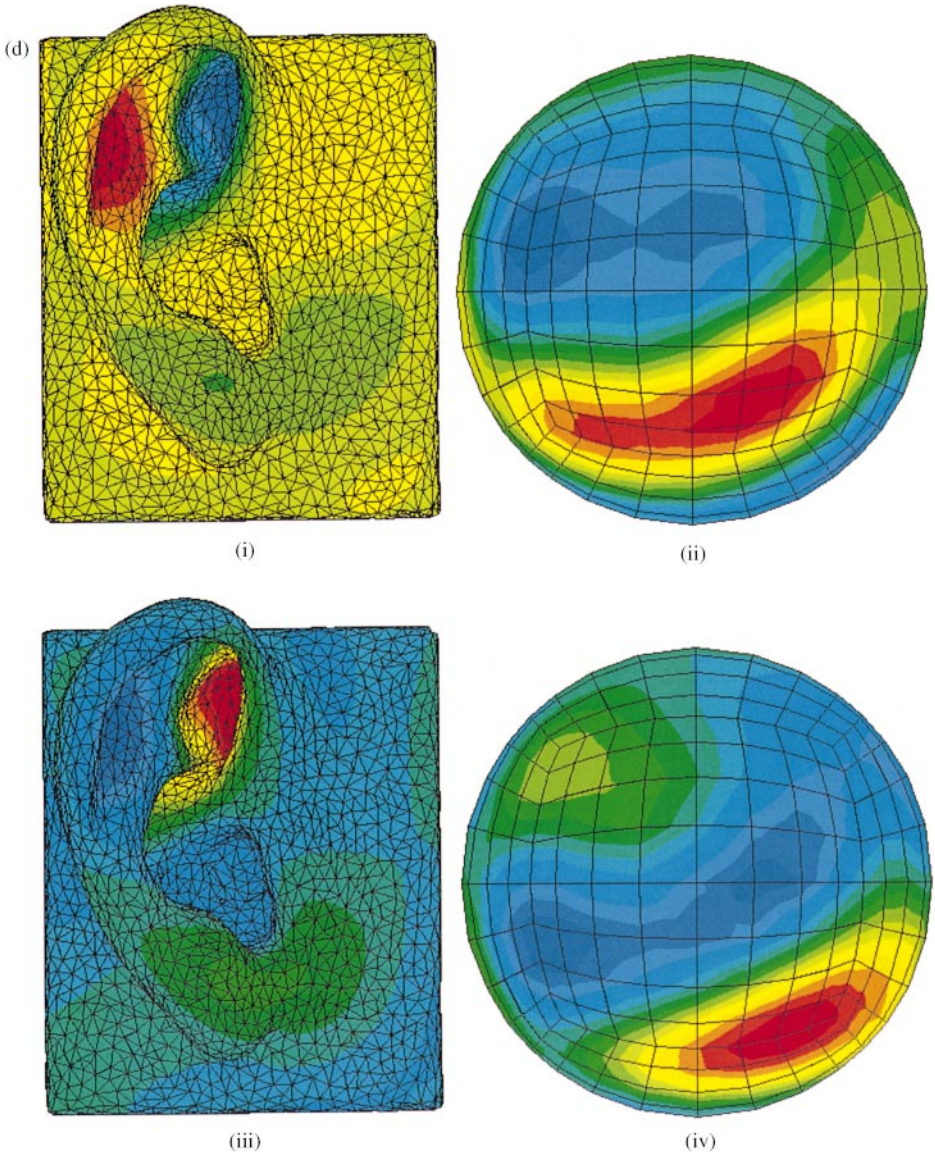

10 300 Hz/σ_2	Minimum scale (blue)	Maximum scale (red)
(i) Real (v)	−8·548e–02	4·347e–02
(ii) Real (u)	−1·131e–01	1·077e–01
(iii) Imag (v)	−1·504e–02	2·562e–02
(iv) Imag (u)	−9·232e–02	1·144e–01

Figure 20. continued

complex modes of this type at, on average, 12 100 and 14 400 Hz). It should be noted that one would not expect to get exactly the same "resonance frequencies" as those found by Shaw since his resonance frequencies were found by exciting the pinna only at grazing incidence and with a "near-field" spherical source. Our spatial basis functions are based on excitations from the whole hemisphere, and near-field effects are eliminated. In addition, it

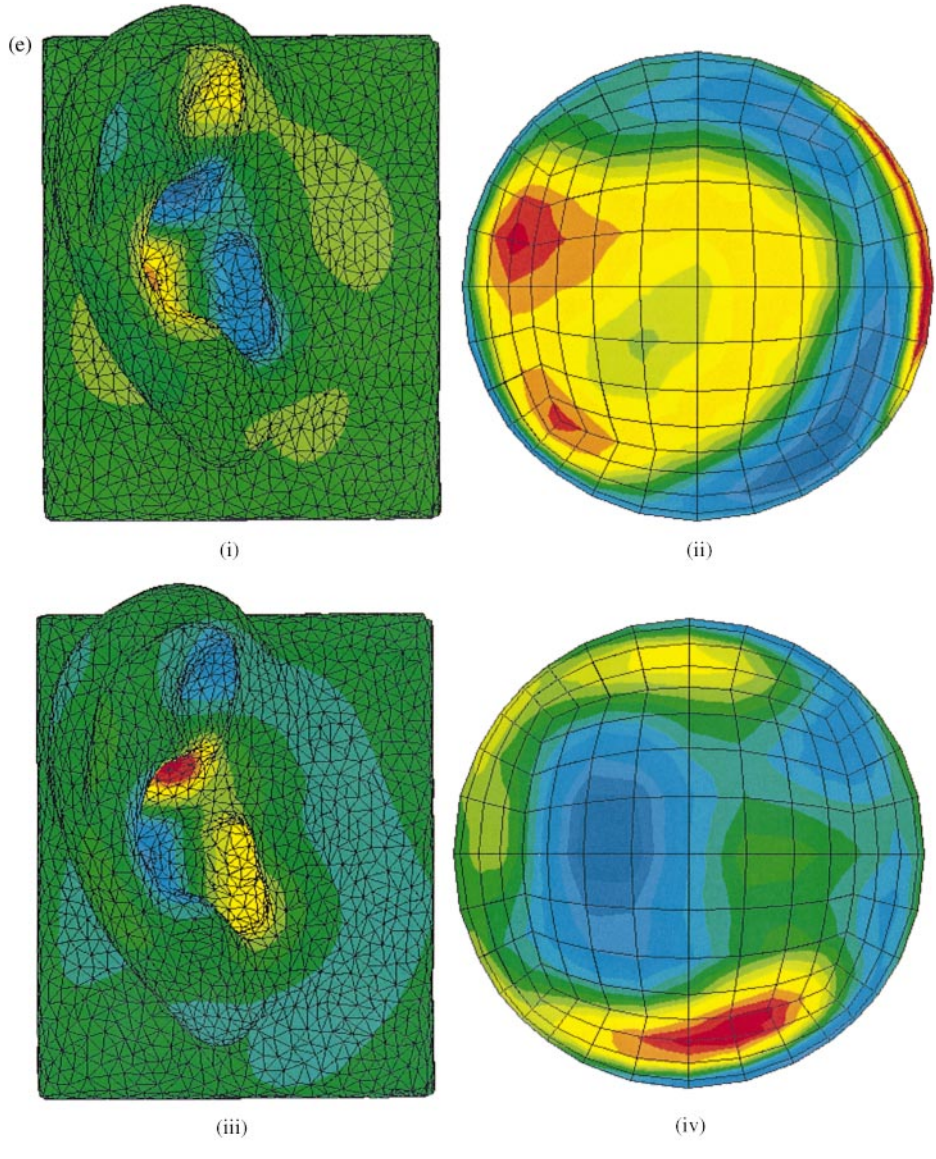

13 800 Hz	Minimum scale (blue)	Maximum scale (red)
(i) Real (v)	−5·947e−02	5·174e−02
(ii) Real (u)	−8·052e−02	1·221e−01
(iii) Imag (v)	−5·710e−02	7·03e−02
(iv) Imag (u)	−1·084e−01	1·085e−01

Figure 20. continued

is important to emphasize that, in arriving at his results, Shaw averaged the response over 10 human pinnae. It is not clear if all of the six modes that were identified by Shaw exist or have similar patterns for each individual pinna since these have not been included in his publications. For example, in a recent study undertaken by the authors, it was found that all six modes indeed appeared in a larger ear (DB65) with similar frequencies to those stated by

Shaw. Since differences appear between male and female pinnae, where for the latter higher resonance frequencies occur, it is not certain if the results presented here should necessarily coincide with the average values found by Shaw.

Finally, it should be re-emphasized that the results produced will necessarily be significantly dependent on the geometrical details of individual pinnae. To date, a total of six different pinnae have been analyzed using the procedure described above and at least the basic patterns of response exhibited by the DB60 are replicated by other ears. However, the associated frequencies of peak response differ by typically 20% and again this is consistent with the results of experimental studies [17–19]. Nevertheless, it does seem possible to build a "reduced order model" of the pinna frequency response by using only a relatively small number of the dominant singular values and their associated basis functions.

6. CONCLUSIONS

A number of numerical simulations have been undertaken in order to examine the connection between the basis functions provided by the singular-value decomposition of matrices of acoustic transfer functions and the basis functions provided by classical acoustical analyses. In particular, it has been found that for radiation from the surface of a sphere to a spherical surface in the far field, the left and right singular vectors associated with the SVD are related to the sampled spherical harmonics by a unitary transformation. This relationship is contingent on the source and field being sampled by dividing the spherical surfaces involved into segments of equal area. The relationship is found not to hold for non-uniform sampling of the surfaces involved.

Some preliminary results have also been presented of the use of the SVD in analyzing the scattering of sound by the human pinna. It is found that the dominant singular value peaks at certain frequencies at which the left and right singular vectors exhibit distinctive spatial patterns. These patterns appear to be connected to the "mode shapes" identified in previous experimental studies of "pinna resonance". The phenomena identified await further investigation.

This paper is dedicated to Professor Philip E. Doak on the occasion of his 80th birthday. The first author (PAN) remains deeply grateful to "PED" for teaching him theoretial acoustics as an MSc. student, for supervising his PhD studies of aerodynamic sound and for his continued friendship and support. The authors also hope that he will approve of their attempt to make some useful connections between "classical acoustics" and modern-day numerical methods.

REFERENCES

1. G. V. Borgiotti 1990 *Journal of the Acoustical Society of America* **88**, 1884–1893. The power radiated by a vibrating body in an acoustic field and its determination from boundary measurements.
2. D. M. Photiadis 1990 *Journal of the Acoustical Society of America* **88**, 1152–1159. The relationship of singular value decomposition to wave-vector filtering in sound radiation problems.
3. M. N. Currey and K. A. Cunefare 1995 *Journal of the Acoustical Society of America* **98**, 1570–1580. The radiation modes of baffled finite plates.
4. S. J. Elliott and M. E. Johnson 1993 *Journal of the Acoustical Society of America* **94**, 2194–2204. Radiation modes and the active control of sound power.

5. W. A. VERONESI and J. D. MAYNARD 1989 *Journal of the Acoustical Society of America* **85**, 588–598. Digital holographic reconstruction of sources with arbitrarily shaped surfaces.
6. P. J. T. FILIPPI, D. HABAULT and J. PIRAUX 1998 *Journal of Sound and Vibration* **124**, 285–296. Noise source modelling and identification procedure.
7. G. T. KIM and B. H. LEE 1990 *Journal of Sound and Vibration* **136**, 245–26. 3-D sound reconstruction and field projection using the Helmholtz integral equation.
8. S. P. GRACE, H. M. ATASSI and W. K. BLAKE 1996 *American Institute of Aeronautics and Astronautics Journal* **34**, 2233–2240. Inverse aeroacoustic problem for a streamlined body, Part 1. Basic formulation.
9. S. P. GRACE, H. M. ATASSI and W. K. BLAKE 1996 *American Institute of Aeronautics and Astronautics Journal* **34**, 2241–2246. Inverse aeroacoustic problem for a streamlined body. Part 2. Accuracy of solutions.
10. P. A. NELSON and S. H. YOON 2000 *Journal of Sound and Vibration*. **233**, 643–668. Estimation of acoustic source strength by inverse methods: Part I. Conditioning of the inverse problem.
11. S. H. YOON and P. A. NELSON 2000 *Journal of Sound and Vibration*. **233**, 669–705. Estimation of acoustic source strength by inverse methods: Part II. Experimental investigation of methods for choosing regularisation parameters.
12. P. A. NELSON 1999 *Proceedings of the 7th International Congress on Sound and Vibration, Copenhagen*, Vol. 1, 7–32. Some inverse problems in acoustics.
13. D. COLTON and R. KRESS 1998 *Inverse Acoustic and Electromagnetic Scattering Theory*. Berlin: Springer-Verlag; second edition.
14. P. M. MORSE and H. FESHBACH 1953 *Methods of Theoretical Physics*, New York: McGraw Hill.
15. P. M. MORSE and K. U. INGARD 1968 *Theoretical Acoustics*. Princeton, NJ: Princeton University Press.
16. G. ARFKEN 1970 *Mathematical Methods for Physicists*. New York: Academic Press; second edition.
17. E. A. G. SHAW 1997 in *Binaural and Spatial Hearing in Real and Virtual Environments* (R. H. Gilkey and T. R. Anderson, editors). Mahwah, NJ; Lawrence Erlbaum Associates. Acoustical features of the human external ear.
18. E. A. G. SHAW 1975. in *Proceedings of the 7th Danavox Symposium* (S. C. Dalsgaard, editor), Scandinavian Audiology supplement 5, 24–50. The external ear: new knowledge in Earmolds and associated problems.
19. E. A. G. SHAW 1979 in *Localisation of Sound: Theory and Applications* (R. W. Gatehouse, editor) 18–29. Groton, CT: Amphora Press. Rayleigh medal lecture: the elusive connection.
20. S. TEMKIN 1981 *Elements of Acoustics*. New York: John Wiley.
21. *MATHEMATICA* 3.0 *Users Manual*, Wolfram Research Inc.
22. *SYSNOISE* 5.4 *Users Manual*, LMS International, Leuven, Belgium.
23. *MATLAB* 5.3 *Users Manual*, Mathworks Inc.
24. KEMAR Dummy Head, Knowles Electronics.
25. B. F. G. KATZ 1998 *Ph.D. Thesis, Pennsylvania State University*. Measurement and calculation of individual head-related transfer functions using a boundary element model including the measurement and effect of skin and hair impedance.
26. Y. KAHANA 2000 *Ph.D. Thesis, University of Southampton*. Numerical modelling of the head related transfer function.